JOURNAL OF PETROLOGY | VOLUME 55 | NUMBER 5 | PAGES 951–976 | 2014 | doi:10.1093/petrology/egu012

Using Multiphase Solid Inclusions to Constrain the Origin of the Baima Fe–Ti–(V) Oxide Deposit, SW China

PING-PING LIU[1], MEI-FU ZHOU[1]*, WEI TERRY CHEN[1], MARIJN BOONE[2,3] AND VEERLE CNUDDE[2]

[1]DEPARTMENT OF EARTH SCIENCES, UNIVERSITY OF HONG KONG, POKFULAM ROAD, HONG KONG, PEOPLE'S REPUBLIC OF CHINA

[2]DEPARTMENT OF GEOLOGY AND SOIL SCIENCES-UGCT, GHENT UNIVERSITY, KRIJGSLAAN 281/S8, 9000 GHENT, BELGIUM

[3]UNIT SUSTAINABLE MATERIALS MANAGEMENT, VITO, MOL 2400, BELGIUM

RECEIVED AUGUST 16, 2013; ACCEPTED MARCH 6, 2014

Multiphase solid inclusions within cumulus silicates, particularly olivine, in Fe–Ti oxide ores from the Lower Zone of the Baima intrusion, Emeishan large igneous province, SW China, have been identified for the first time using 2-D scanning electron microscope and 3-D high-resolution X-ray computed tomography. These inclusions are spherical to subspherical and range from 100 to 300 μm in diameter. They are composed dominantly of titanomagnetite and ilmenite with minor apatite, hornblende, phlogopite and pyrrhotite. The titanomagnetite in the inclusions has a low Cr content (<700 ppm) similar to the interstitial titanomagnetite, suggesting that these inclusions cannot be early crystallized mineral aggregates. In contrast, the spherical shape of these inclusions provides evidence of early trapped liquids from which these minerals crystallized. Based on the composition and modal proportions of the daughter mineral phases within the inclusions, the trapped liquids are estimated to have 82·1–59·6 wt % FeO^T, 11·4–18·5 wt % TiO_2, 2·69–6·12 wt % Al_2O_3, 1·40–4·47 wt % MgO, 0·87–4·93 wt % SiO_2 and ~1 wt % volatiles including F, S, Cl, P and H_2O. Such a liquid composition deviates substantially from that of the slightly evolved ferrobasaltic magmas inferred to be parental to the Fe–Ti–(V) oxide-bearing mafic–ultramafic intrusions of the Emeishan large igneous province. It is thus speculated that these trapped liquids are immiscible Fe–Ti-rich melts formed upon cooling of ferrobasaltic magma. The net-textured and disseminated oxide ores have titanomagnetite compositions similar to those in the inclusions, suggesting that the oxide ores of the Baima intrusion also formed from Fe–Ti-rich melts immiscibly separated from ferrobasaltic magmas. We propose that immiscible Fe–Ti-rich liquids with high density percolated down through crystal-bearing silicate magma and crystallized an interconnected Fe–Ti oxide network interstitial to olivine, plagioclase and clinopyroxene. This study highlights that immiscible separation of Fe–Ti-rich liquids from ferrobasaltic magmas is an important mechanism in the formation of magmatic Fe–Ti–(V) oxide deposits hosted in mafic–ultramafic layered intrusions.

KEY WORDS: *3-D X-ray computed tomography; Baima intrusion; liquid immiscibility; multiphase solid inclusion; net-textured oxide ore; SW China*

INTRODUCTION

Fe–Ti oxide ores, commonly rich in apatite, are often associated with massif-type anorthosites and mafic–ultramafic layered intrusions. Their origin has been variously suggested to result from fractional crystallization and gravitational crystal settling from ferrobasaltic magmas (e.g. Wager & Brown, 1968; Duchesne, 1999; Charlier *et al.*, 2006, 2008; Pang, 2008*a*, 2008*b*, 2009) or crystallization from Fe–Ti–P-rich liquids segregated from evolved,

*Corresponding author. Telephone: +852 28578251. Fax: +852 25176912. E-mail: mfzhou@hku.hk

© The Author 2014. Published by Oxford University Press. All rights reserved. For Permissions, please e-mail: journals.permissions@oup.com

Downloaded from https://academic.oup.com/petrology/article/55/5/951/1496553 by guest on 20 August 2022

Si-rich, conjugate liquids (e.g. Bateman, 1951; Ripley *et al.*, 1998; Jakobsen *et al.*, 2005; Zhou *et al.*, 2005, 2013; Namur *et al.*, 2012; Wang & Zhou, 2013). Immiscibility of Fe–Ti–P-rich melts has been recognized as an important mechanism for the formation of nelsonites and Fe–Ti oxides in massif anorthosites (Philpotts, 1967; Kolker, 1982; Ripley *et al.*, 1998; Clark & Kontak, 2004; Chen *et al.*, 2013), and of titanomagnetite–apatite-rich ores hosted in gabbros or gabbronorites in the upper part of large layered intrusions such as the Bushveld Complex and the Skaergaard intrusion (e.g. Reynolds, 1985*a*, 1985*b*; Von Gruenewaldt, 1993; Jakobsen *et al.*, 2005; VanTongeren & Mathez, 2012). Recent work has demonstrated that silicate liquid immiscibility does not necessarily occur at the very end of crystallization, but earlier, soon after the start of magnetite and ilmenite crystallization at the transition from the Lower to the Middle Zones of the Skaergaard intrusion where apatite is not an abundant phase (Veksler *et al.*, 2007; Veksler, 2009; Jakobsen *et al.*, 2011). The question concerning the origin of these rocks is thus whether they formed by normal fractional crystallization processes from a single silicate magma or from Fe-rich melts immiscibly segregating from a Si-rich magma, and at what stage immiscibility can occur.

Evidence for liquid immiscibility is unlikely to be preserved in layered intrusions because the rocks have undergone lengthy and complex cooling and readjustment processes before and after solidification. Entrapment of minerals and melts, on the other hand, can provide robust information about the early stage of magma evolution (e.g. Roedder & Weiblen, 1970; Schiano *et al.*, 1997; Jakobsen *et al.*, 2005; Pang *et al.*, 2008*a*). In the Permian Emeishan large igneous province (ELIP), the Panzhihua, Hongge and Baima mafic–ultramafic intrusions in the Panxi (Panzhihua–Xichang) region host significant Fe–Ti–(V) oxide ores in their lower or middle parts. Proposed models for the origin of the oxide ores include immiscible separation of Fe-rich and Si-rich liquids (Zhou *et al.*, 2005; Wang & Zhou, 2013), early crystallization and gravitational settling of oxides from the same ferrobasaltic magma along with silicate minerals (Pang *et al.*, 2008*a*, 2008*b*, 2009; Shellnutt & Pang, 2012) and fractional crystallization from a magma flow-through system with repeated magma replenishment (Bai *et al.*, 2012; Zhang *et al.*, 2012; Song *et al.*, 2013). These diverse models highlight the importance of investigating Fe–Ti oxide ore-forming processes in mafic–ultramafic intrusions.

In this contribution, we identify the presence of spherical to subspherical multiphase solid inclusions within cumulus silicates of net-textured and disseminated Fe–Ti oxide ores in the Lower Zone of the Baima layered intrusion. High-resolution X-ray computed tomography (CT) was used to obtain the three-dimensional (3-D) morphology and spatial distribution of daughter mineral phases within the inclusions. Together with scanning electron microscope (SEM) and electron microprobe analysis (EMPA), single mineral phases were identified and their compositions determined. These spherical to subspherical multiphase solid inclusions provide unique and robust evidence for the entrapment of Fe–Ti-rich liquids. We show that the interstitial Fe–Ti oxides may have crystallized from compositionally similar melts. These new findings indicate that immiscible Fe–Ti-rich liquids are responsible for the net-textured and disseminated ores in the Lower Zone of the Baima intrusion.

GEOLOGICAL BACKGROUND

The Emeishan large igneous province

The ~260 Ma ELIP covers an area of $\sim 5 \times 10^5$ km^2 in SW China and northern Vietnam, bounded by the Tibetan Plateau to the west and the Yangtze Block to the east (Chung *et al.*, 1998; Fig. 1). It consists of coeval flood basalts, mafic–ultramafic intrusions and associated felsic plutons that were erupted or emplaced within a short period of time at the Permian–Triassic boundary (Chung *et al.*, 1998; Song *et al.*, 2001; Xu *et al.*, 2001; Zhou *et al.*, 2002). The ELIP continental flood basalts range in thickness from ~5 km in the west to a few hundred meters in the east (Chung & Jahn, 1995), and have been subdivided into low-Ti and high-Ti series (Xu *et al.*, 2001). Associated mafic–ultramafic intrusions are economically valuable for their Ni–Cu–platinum group element (PGE) sulfide, Fe–Ti–(V) oxide or PGE mineralization. Fe–Ti–(V) oxide-bearing mafic–ultramafic rocks are considered to be cogenetic with the high-Ti basalts, which have high Ti/Y (>500) and FeO^T (>12%), whereas the Ni–Cu–(PGE) sulfide-bearing ultramafic rocks are petrogenetically linked to the low-Ti basalts, which have low Ti/Y (<500) and FeO^T (<12%) (Xu *et al.*, 2001; Xiao *et al.*, 2004; Wang *et al.*, 2007; Zhou *et al.*, 2008; Song *et al.*, 2009).

Economically important Fe–Ti–(V) oxide-bearing mafic–ultramafic intrusions in the Panxi region are exposed along north–south-trending fault systems and spatially associated with coeval granite and syenite (Fig. 1). The Hongge, Baima and Panzhihua intrusions contain the largest Fe–Ti–(V) oxide deposits with ore reserves of 4572 Mt, 1497 Mt, and 1333 Mt, respectively (Ma *et al.*, 2003). Oxide ores of the Baima intrusion have an average grade of 34·7 wt % FeO^T, 6·19 wt % TiO_2 and 0·26 wt % V_2O_5 (Sichuan Bureau of Geology and Mineral Resources, 2007).

Field relations of the Baima intrusion

The ~16 km long and 0·13–2·2 km wide Baima intrusion strikes broadly north–south and dips 15–70° west. It is separated by a series of NE–SW-trending faults into segments, which are named from north to south Xiajiaping, Jijiping, Tianjiacun, Qinggangping and Mabinglang

Downloaded from https://academic.oup.com/petrology/article/55/5/951/1496553 by guest on 20 August 2022

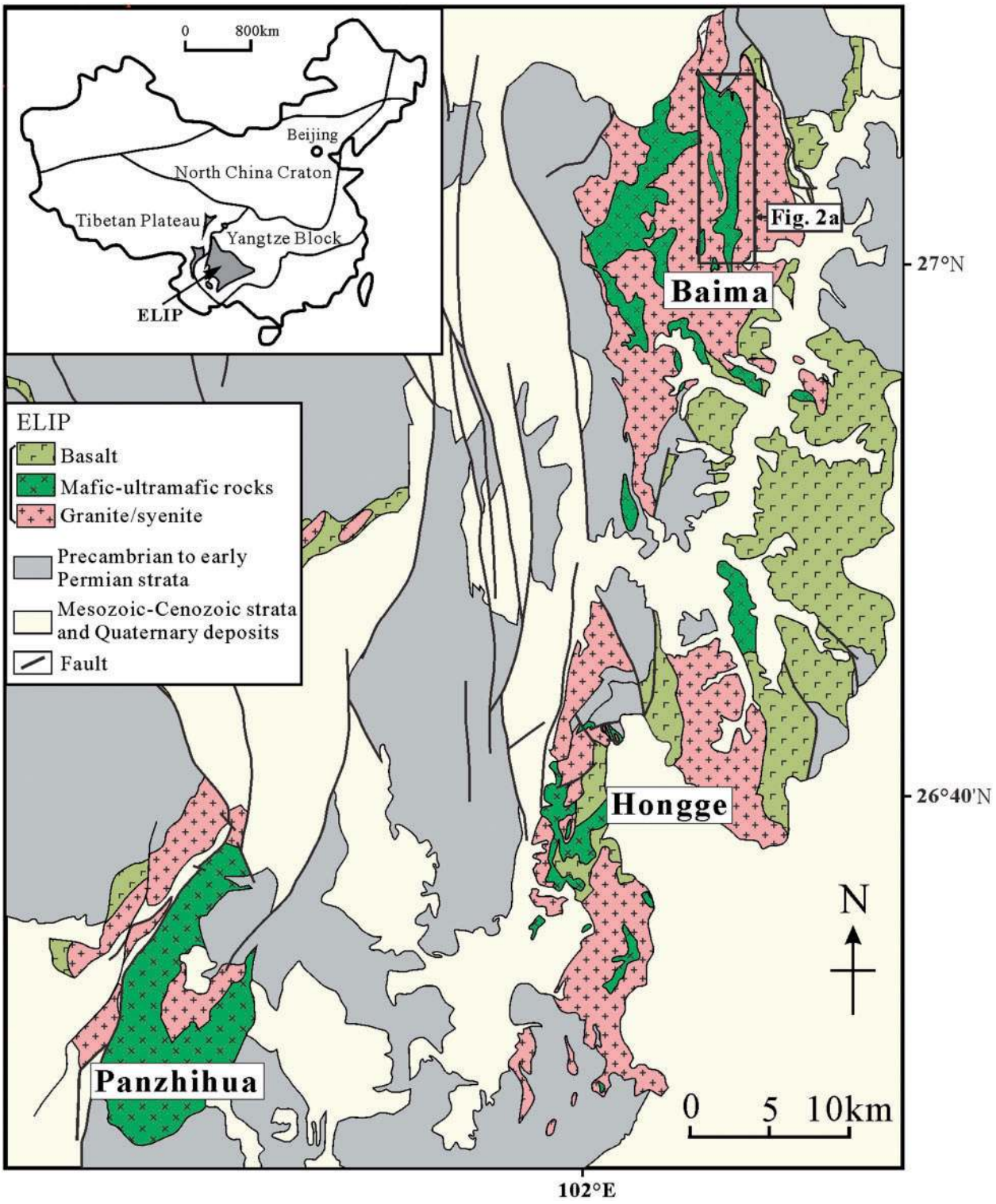

Fig. 1. Simplified regional geology of the Panxi area, Emeishan large igneous province, SW China, showing the distribution of mafic–ultramafic intrusions that host Fe–Ti–(V) oxide ore deposits. Modified after Pang *et al.* (2008*b*). The rectangle shows the location of Fig. 2a.

Downloaded from https://academic.oup.com/petrology/article/55/5/951/1496553 by guest on 20 August 2022

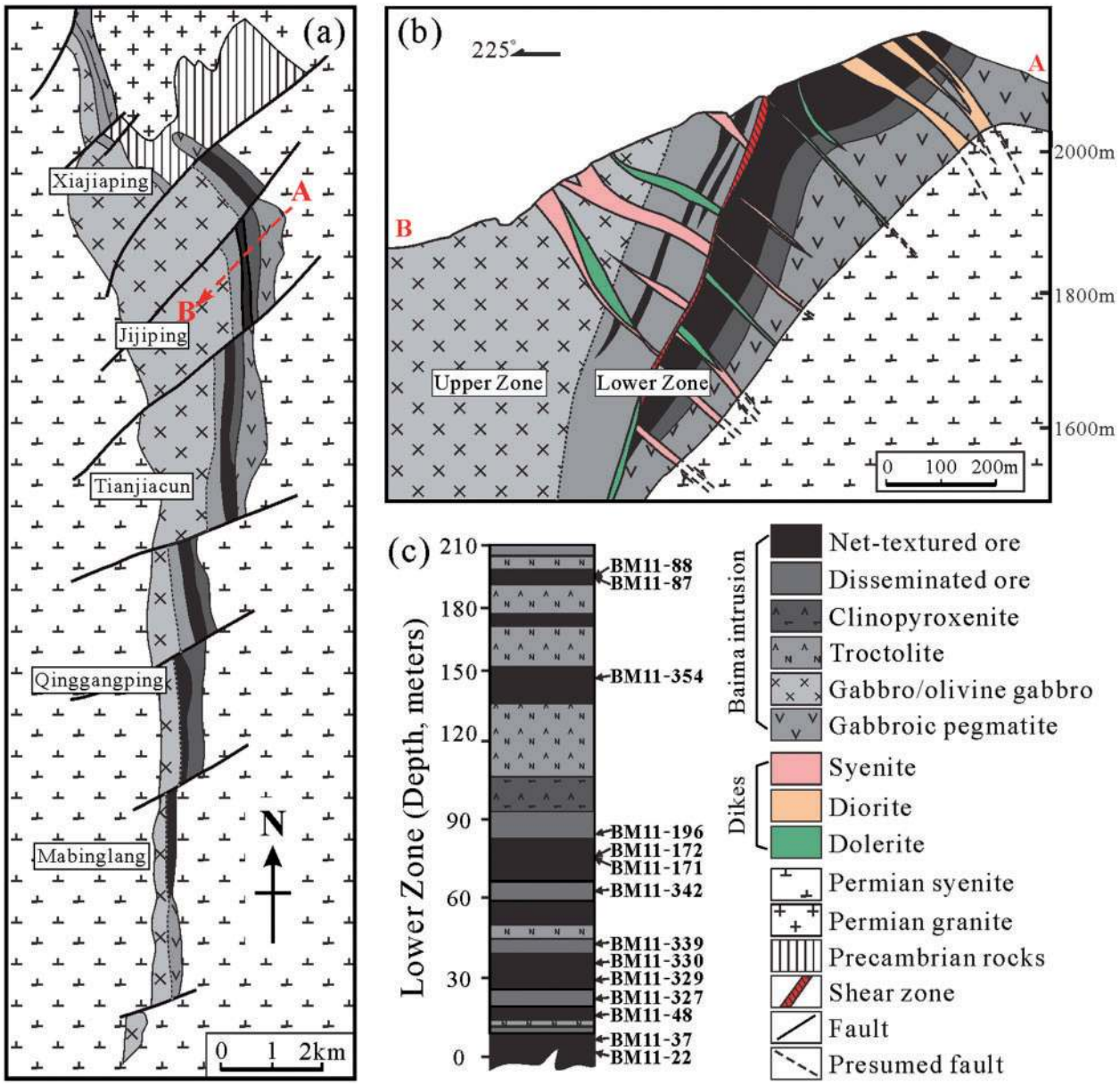

Fig. 2. Details of the geology of the Baima intrusion, SW China. (a) Simplified map view of the Baima mafic–ultramafic intrusion (modified after Chen, 1990). (b) A representative cross-section in the Jijiping segment showing the distribution and morphology of rock types and ores in the Baima intrusion. The location of the section is indicated in (a). The dotted line indicates the boundary between the Lower and Upper Zones. (c) A simplified stratigraphic section of the Lower Zone of the Baima intrusion showing the location of the analysed samples.

(Fig. 2a), and intrudes marble, schist and migmatitic granite of the Precambrian Huili Group and carbonate of the Sinian Dengying Formation. From the base upward, the Baima intrusion has been divided into a Lower and an Upper Zone (Zhang *et al.*, 2012; Liu *et al.*, 2014). The 180–350 m thick Lower Zone consists mainly of alternating ultramafic rocks and Fe–Ti oxide ore layers, whereas the <1500 m thick Upper Zone is composed of isotropic gabbro, olivine gabbro and apatite-bearing gabbro (Fig. 2a and b).

PETROGRAPHY

Lower Zone

The Lower Zone contains conformable layers of Fe–Ti oxide-bearing troctolite, olivine clinopyroxenite and Fe–Ti oxide ores (Fig. 2c). Troctolite is composed of ~30 vol. % olivine, ~40 vol. % plagioclase, 10–20 vol. % Fe–Ti oxides (titanomagnetite and ilmenite), and <10 vol. % hornblende, apatite and sulfides. Olivine clinopyroxenite consists of ~35 vol. % clinopyroxene, ~20 vol. %

Downloaded from https://academic.oup.com/petrology/article/55/5/951/1496553 by guest on 20 August 2022

plagioclase, ~25 vol. % olivine, and ~10 vol. % Fe–Ti oxides. Hornblende, apatite and sulfides are accessory minerals and account for less than 10 vol. %. The ultramafic rocks are fine- to medium-grained and display orthocumulate textures. Olivine is typically subhedral to euhedral, and varies in diameter from 0·3 to 1·5 mm. Euhedral clinopyroxene is generally 0·5–1 mm and has a well-developed schiller structure represented by exsolution of rhombic opaque minerals (probably magnetite) along two intersecting planes. Plagioclase is tabular to platy with irregular wavy edges. Apatite occurs as euhedral hexagonal crystals and varies from 70 to 150 μm in size. In contrast to these cumulus silicate minerals, hornblende occurs as an ~50 μm wide rim surrounding plagioclase or, less commonly, clinopyroxene.

Fe–Ti oxide ores display large variations in modal proportions of minerals and thus are divided into disseminated ores with 20–40 mol % Fe–Ti oxides and net-textured ores with >40 mol % Fe–Ti oxides. The oxide ores are composed of cumulus olivine, clinopyroxene and plagioclase, with interstitial Fe–Ti oxides (Fig. 3a–d). In the net-textured ores, Fe–Ti oxides form an interconnected network enclosing silicate cumulates. Apatite, sulfides and hornblende are present as accessory minerals. Sub- to euhedral olivine is 1–1·5 mm in diameter and ranges from 5 to 30 vol. %. Small olivine grains are locally enclosed in titanomagnetite and ilmenite (Fig. 3e and f). Clinopyroxene is usually subhedral and contains abundant schiller exsolution of Fe–Ti oxides. Plagioclase is commonly tabular and embayed. Titanomagnetite exhibits cloth and trellis exsolution of ilmenite and aluminous spinel, resulting from subsolidus re-equilibration. Ilmenite also occurs as external granular grains. Aluminous spinel commonly occurs at the contact between titanomagnetite and ilmenite (Fig. 3e and f).

Upper Zone

The isotropic gabbro and olivine gabbro of the Upper Zone consist of subhedral clinopyroxene (15–25 vol. %), plagioclase (60–70 vol. %) and olivine (<10 vol. %), with minor (<10 vol. %) Fe–Ti oxides and hornblende. Hornblende occurs as coronae at the contact between plagioclase or clinopyroxene and Fe–Ti oxides. Olivine grains are relatively small and anhedral and do not have mineral inclusions. Apatite (<5 vol. %) is present at the higher level of the Upper Zone.

SAMPLES AND METHODS

Samples

Representative samples selected for 2-D SEM and 3-D X-ray CT analysis include net-textured and disseminated ores from both the lower and upper parts of the Lower Zone (Table 1). The chemical compositions of the constituent minerals were obtained for a number of samples from the lower to the upper parts of the Lower Zone.

SEM images

Scanning electron microscope images were obtained using a Hitachi S-3400N variable pressure scanning electron microscope (SEM) at the University of Hong Kong. The SEM has a tungsten filament emitter with a resolution of ~5 nm at 30 kV. The image is acquired under an operating voltage of 20 kV and pressure of 60–100 Pa. Compositional mapping was conducted using a highly sensitive four-segment backscattered electron (BSE) detector.

3-D morphologies

X-ray CT was used to visualize the structure of the mineral inclusions in olivine within the oxide ores in three dimensions in a non-destructive manner to ensure that the inclusions identified from the 2-D SEM images were isolated inclusions. The 3-D characterization was performed at Ghent University (Belgium) using a custom-built CT scanner setup with a FeinFocus FXE160.51 transmission-type X-ray tube combined with a Varian PaxScan 2520 V a-Si flat panel detector for image acquisition (Masschaele *et al.*, 2007). The X-ray source was operated at 90 kV and beam hardening artefacts were reduced with a 1 mm thick aluminum filter. The acquired radiographs were reconstructed to a 3-D volume using the reconstruction software Octopus (Vlassenbroeck *et al.*, 2007); the resulting 3-D images have an isotropic voxel size of $1{\cdot}5^3$ μm^3. The 3-D image gives a representation of the local attenuation coefficient in grayscale. The resultant images were visualized using the software package VGStudio and further analyzed using the 3-D analysis software package Morpho+ (Brabant *et al.*, 2011).

Chemical compositions

Major element compositions of silicates, apatite and Fe–Ti oxides were acquired using a JEOL JXA-8100 electron microprobe (EMP) at the Key Laboratory of Isotopic Geochemistry, Guangzhou Institute of Geochemistry, Chinese Academy of Sciences. The analyses were carried out using a voltage of 15 kV and a beam current of 20 nA, focused to a spot of 1 μm. Peak and background counting times for major elements were 20 s and 10 s, respectively, whereas those for trace elements were 40 s and 20 s, respectively. The standards used for oxide analyses were albite for Si, Na and Al, plagioclase for Ca, potassium feldspar for K, garnet for Fe and rutile for Ti. The precisions of the major element and trace element determinations were better than 2% and 5%, respectively. Matrix corrections were performed using ZAF procedures (Jurek & Hulínský, 1980).

An average composition of titanomagnetite that contains ilmenite exsolution lamellae was determined by laser

Downloaded from https://academic.oup.com/petrology/article/55/5/951/1496553 by guest on 20 August 2022

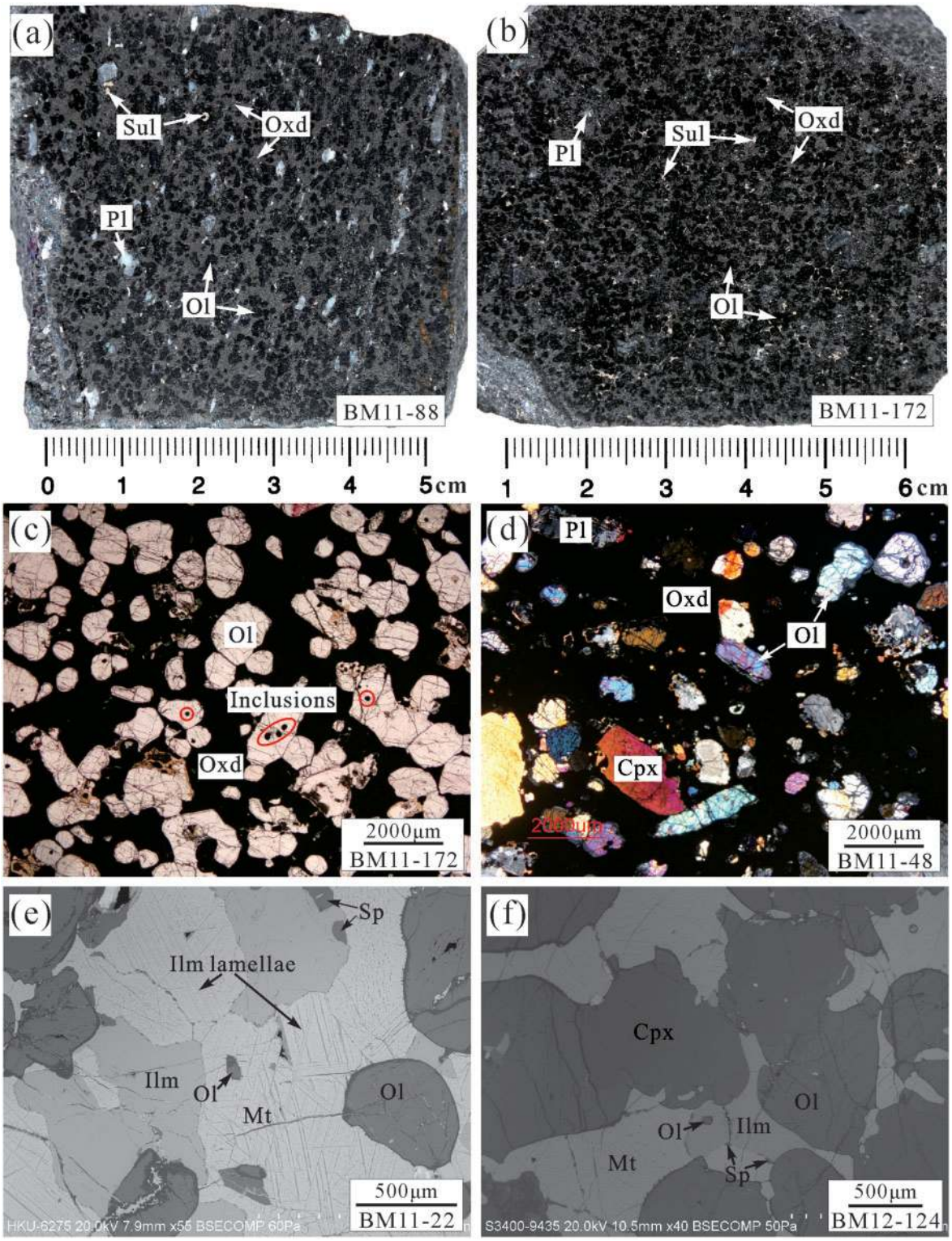

Fig. 3. (a) and (b) Sawn and polished slabs of net-textured oxide ores from the Lower Zone of the Baima intrusion (samples BM11-88 and BM11-172, respectively). (c) and (d) Photomicrographs of net-textured ores (BM11-172 and BM11-48) under plane polars and crossed polars, respectively. Opaque Fe–Ti oxides occur as an interconnected network enclosing cumulus olivine, clinopyroxene and plagioclase. Rounded mineral inclusions occur in olivine grains. (e) and (f) Scanning electron microscope (SEM) images of olivine enclosed in titanomagnetite and ilmenite in oxide ores (samples BM11-22 and BM12-124, respectively) from the Lower Zone. Cpx, clinopyroxene; Ilm, ilmenite; Mt, titanomagnetite; Ol, olivine; Oxd, oxide minerals (titanomanetite, ilmenite and spinel); Pl, plagioclase; Sp, spinel; Sul, sulfide.

Downloaded from https://academic.oup.com/petrology/article/55/5/951/1496553 by guest on 20 August 2022

Table 1: Summary of the oxide ore samples analysed within the Lower Zone of the Baima intrusion: their stratigraphic position, modal mineralogy and texture

Stratigraphic depth (m)*	Sample no.	Modal mineralogy (mol %)				Ore texture
		Ol	Cpx	Pl	Fe–Ti oxides	
5	BM11-22	53	2	5	40	Net-texture
8	BM11-37	50	2	8	40	Net-texture
15	BM11-48	30	5	5	60	Net-texture
22	BM11-327	50	5	15	30	Disseminated
30	BM11-329	35	2	3	60	Net-texture
35	BM11-330	45	5	10	40	Net-texture
42	BM11-339	40	15	10	35	Disseminated
62	BM11-342	40	10	20	30	Disseminated
75	BM11-171/172†	55	2	3	40	Net-texture
84	BM11-196	35	5	10	50	Net-texture
145	BM11-354	50	3	7	40	Net-texture
195	BM11-87/88†	35	10	15	40	Net-texture

Cpx, clinopyroxene; Ol, olivine; Pl, plagioclase; Fe–Ti oxides include titanomagnetite, ilmenite and spinel.
*Stratigraphic depth can be referred to Fig. 2c.
†Samples BM11-171 and BM11-172 are from the same slice; so are samples BM11-87 and BM11-88.

ablation inductively coupled plasma mass spectrometry (LA-ICP-MS), using a Resonetic M50 193 nm Excimer laser system coupled to Thermo PQ Excell inductively coupled plasma mass spectrometer system at the Department of Earth Sciences, the University of Hong Kong. USGS standard reference materials, BHVO-2G, BCR-2G and BIR-1G, were used as external standards and ^{57}Fe as an internal standard to calibrate element contents (Liu *et al.*, 2008). Each analysis includes 20 s for measuring the gas blank and 45 s for data acquisition using a 40 μm diameter spot size at 6 Hz with an energy of ~100 mJ per pulse. Quality control of time-dependent drift of sensitivity and mass discrimination was monitored by analysing GSE-1G, repeated after every eight analyses. The off-line data processing was performed using the program ICPMSDataCal (Liu *et al.*, 2008).

RESULTS

Embayed silicate minerals

Many cumulus clinopyroxene and plagioclase grains in the oxide ores have embayed or skeletal textures. Brown hornblende is commonly present as ~50 μm wide monomineralic rims at the contact of Fe–Ti oxides and embayed clinopyroxene or plagioclase (Fig. 4). In some samples, relics of narrow edges of plagioclase and clinopyroxene replaced by dark brown hornblende are preserved, which are barely visible under crossed polars (Fig. 4a and b).

3-D morphologies of net-textured oxide ores

X-ray CT analysis shows that the 3-D distribution of net-textured oxide ores (3-D animations of the samples are available in Supplementary Video 1; supplementary material is available at http://www.petrology.oxfordjournals.org) is characterized by oxide minerals occurring as interconnected networks enclosing olivine, plagioclase and clinopyroxene (Fig. 5a). The oxides form complex shapes around silicate crystals on scales greater than the sample size (i.e. 10 mm length). They fill in the interstitial spaces between silicates, resulting in an Fe–Ti oxide net- or matrix-texture (Fig. 5b). In contrast, subspherical silicate minerals in net-textured ores occur as isolated grains, most of which are not connected (Fig. 5c).

Petrography and 3-D morphologies of the inclusions

Two-dimensional SEM images show that the multiphase solid inclusions in olivine from net-textured to disseminated ores have rounded to subrounded shapes and range from 100 to 300 μm in diameter. Two types of inclusions can be identified. One consists of titanomagnetite, ilmenite and minor spinel (Fig. 6). The other type is less abundant and contains mainly titanomagnetite, ilmenite, spinel, and <1 vol. % hornblende, mica, apatite and sulfides (Fig. 7). In a few samples, the inclusions display zonal distributions of minerals characterized by titanomagnetite

Downloaded from https://academic.oup.com/petrology/article/55/5/951/1496553 by guest on 20 August 2022

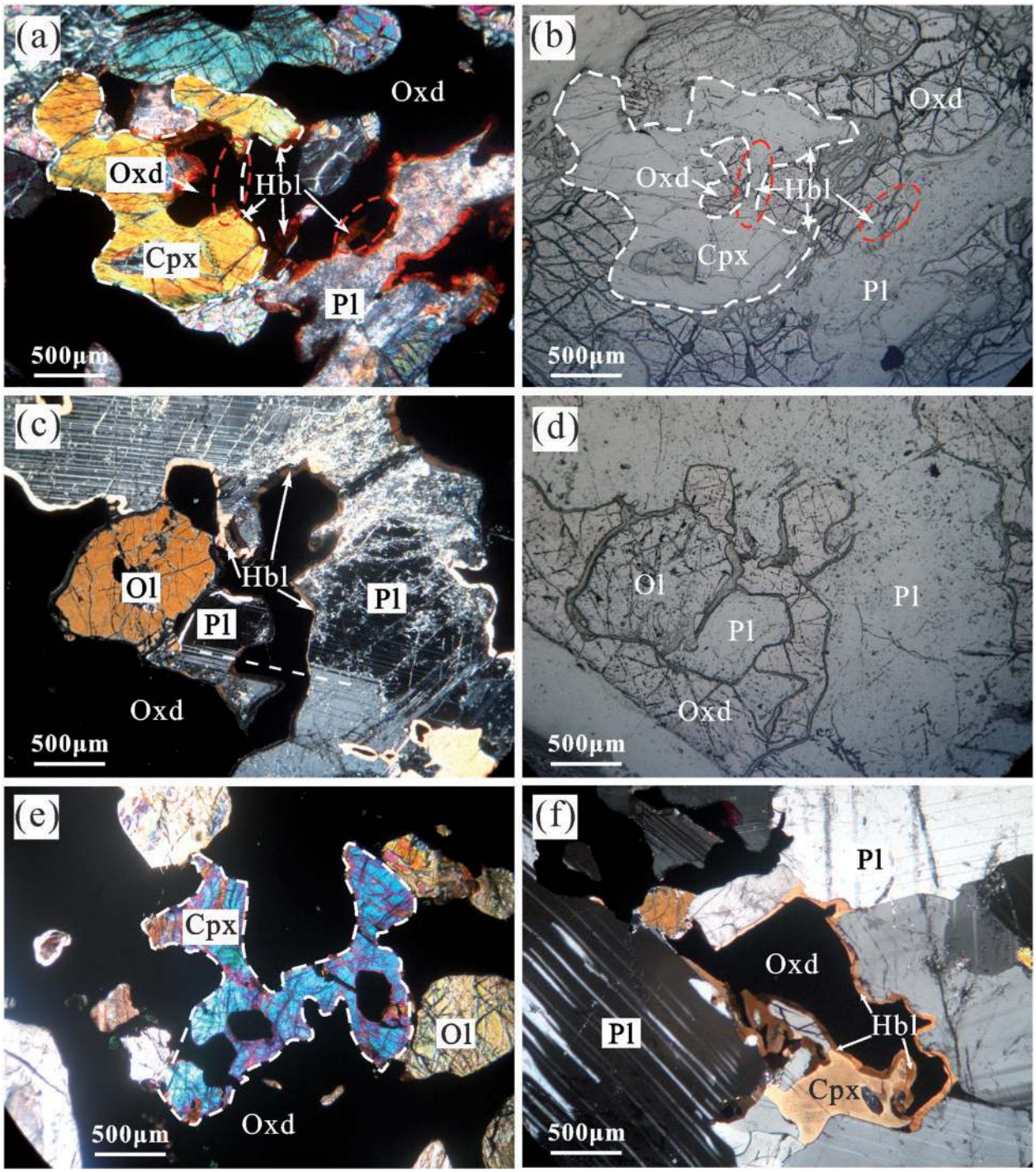

Fig. 4. Photomicrographs of microstructures observed in the oxide ores of the Lower Zone (a–e) and a gabbro of the Upper Zone (f) of the Baima intrusion. (a) and (b) The same image taken under crossed polars and reflected light, respectively, showing the embayed clinopyroxene with hornblende rim in contact with Fe–Ti oxides (sample BM11-339). Dark brown hornblende, which is barely visible under crossed polars, replaces narrow clinopyroxene or plagioclase rims. (c) and (d) The same image taken under crossed polars and reflected light, respectively, showing embayed plagioclase with a narrow hornblende rim in contact with Fe–Ti oxides (sample BM11-87). (e) Image taken under crossed polars showing skeletal clinopyroxene set in net-textured Fe–Ti oxides (sample BM11-329). (f) Image taken under crossed polars showing a hornblende rim at the contact of Fe–Ti oxide with plagioclase and clinopyroxene in gabbro (sample BM11-385). Cpx, clinopyroxene; Hbl, hornblende; Ol, olivine; Oxd, oxide minerals (titanomanetite, ilmenite and spinel); Pl, plagioclase.

Downloaded from https://academic.oup.com/petrology/article/55/5/951/1496553 by guest on 20 August 2022

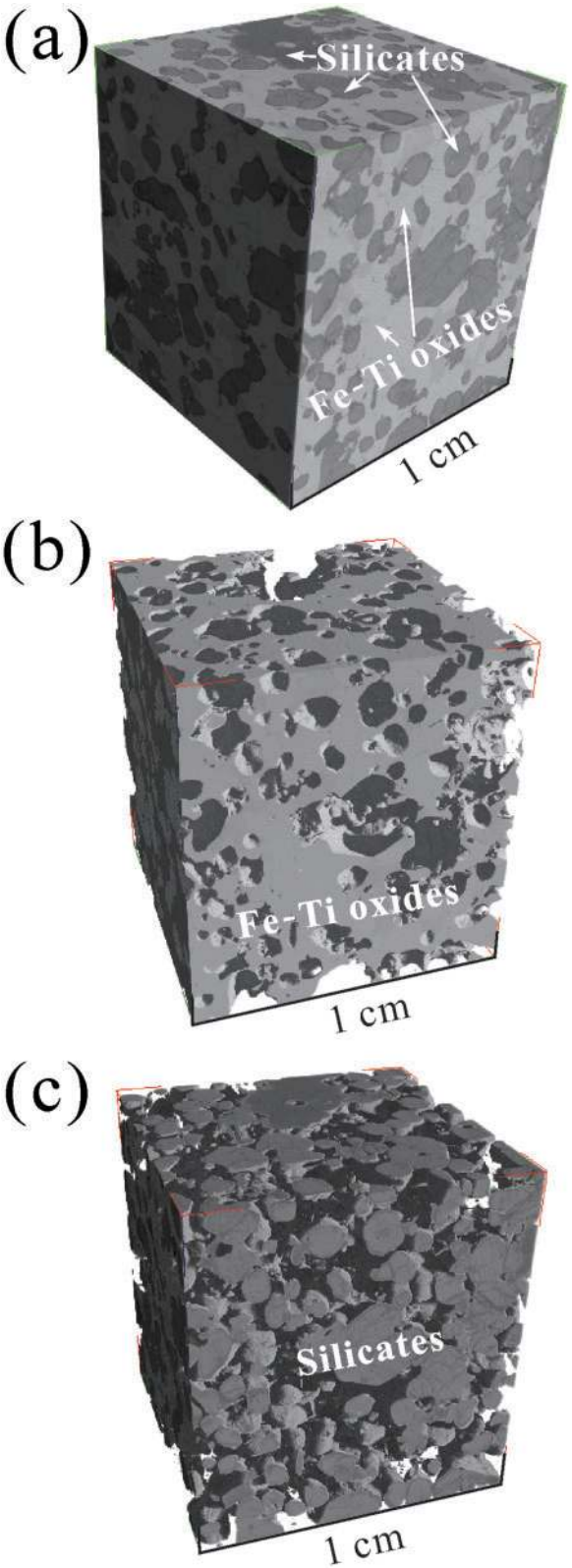

Fig. 5. The 3-D distribution of cumulus silicates and Fe–Ti oxides in the oxide ore (sample BM11-88) from the Lower Zone of the Baima intrusion based on the output from CT scans. The 3-D image gives a representation of the local attenuation coefficient in grayscale. The local attenuation coefficient is a function of the energy of the X-rays and the density and atomic number of the minerals in the rock. Olivine in the scanned sample has an intermediate attenuation coefficient or grayscale value. In comparison, titanomagnetite, ilmenite and sulfide have a higher attenuation coefficient, which results in a more white–grey shade. Plagioclase, clinopyroxene, spinel, mica and hornblende, on the other hand, have a lower attenuation coefficient and thus a lower greyscale value with respect to olivine. (a) Volume rendering of the net-textured ore sample showing the distribution and morphology of the cumulus silicates (dark gray) and the Fe–Ti oxides (light grey). (b) A 3-D visualization of Fe–Ti oxides showing that the Fe–Ti oxides form an interconnected network. (c) A 3-D visualization of cumulus silicates showing that the silicates occur as isolated grains.

in the outer zone and apatite, mica, hornblende and sulfide in the inner zone (Fig. 7a–c). Element mapping shows that the daughter minerals in the inclusions are homogeneous in composition (Fig. 8). Titanomagnetite is rounded in shape and other minerals are also anhedral. Ilmenite occurs either as exsolution lamellae within titanomagnetite, or as irregular grains. Small patches of spinel are commonly distributed along the contact between titanomagnetite and other minerals.

The 3-D CT reconstruction of the oxide ores shows that the inclusions are entirely enclosed in silicates (Fig. 9; 3-D animations of the inclusions are available in Supplementary Video 2). High-resolution 3-D X-ray CT observation demonstrates that the microinclusions are globules of mineral aggregates in silicates, ruling out the possibility of external veinlets connecting with the Fe–Ti oxide network interstitial to the silicates. These inclusions are subspherical to spherical in shape and contain a mineral assemblage of silicates and Fe–Ti oxides. The Fe–Ti oxides are subspherical to spherical and volumetrically dominant (up to 99 vol. %). Variable amounts (1–25 vol. %) of silicate minerals are either enclosed in the Fe–Ti oxides (Fig. 9a and b) or connected to the host silicates (Fig. 9c).

Mineral chemistry

Compositions of apatite, mica, sulfide, hornblende and titanomagnetite in the multiphase solid inclusions were analyzed in oxide ore samples from the Lower Zone of the Baima intrusion, along with interstitial titanomagnetite in the Lower Zone, and hornblende rims in oxide ores of the Lower Zone and (olivine) gabbros of the Upper Zone for comparison.

Titanomagnetite

Major element compositions of titanomagnetite were analyzed by EMP in relatively homogeneous spots devoid of major ilmenite and spinel exsolution. Titanomagnetite in the inclusions has similar amounts of MgO (0·1–3·5 wt %), Al_2O_3 (0·1–3·5 wt %), V_2O_3 (0·2–0·9 wt %), TiO_2 (10–20 wt %) and FeO (30–50 wt %) to the interstitial

Downloaded from https://academic.oup.com/petrology/article/55/5/951/1496553 by guest on 20 August 2022

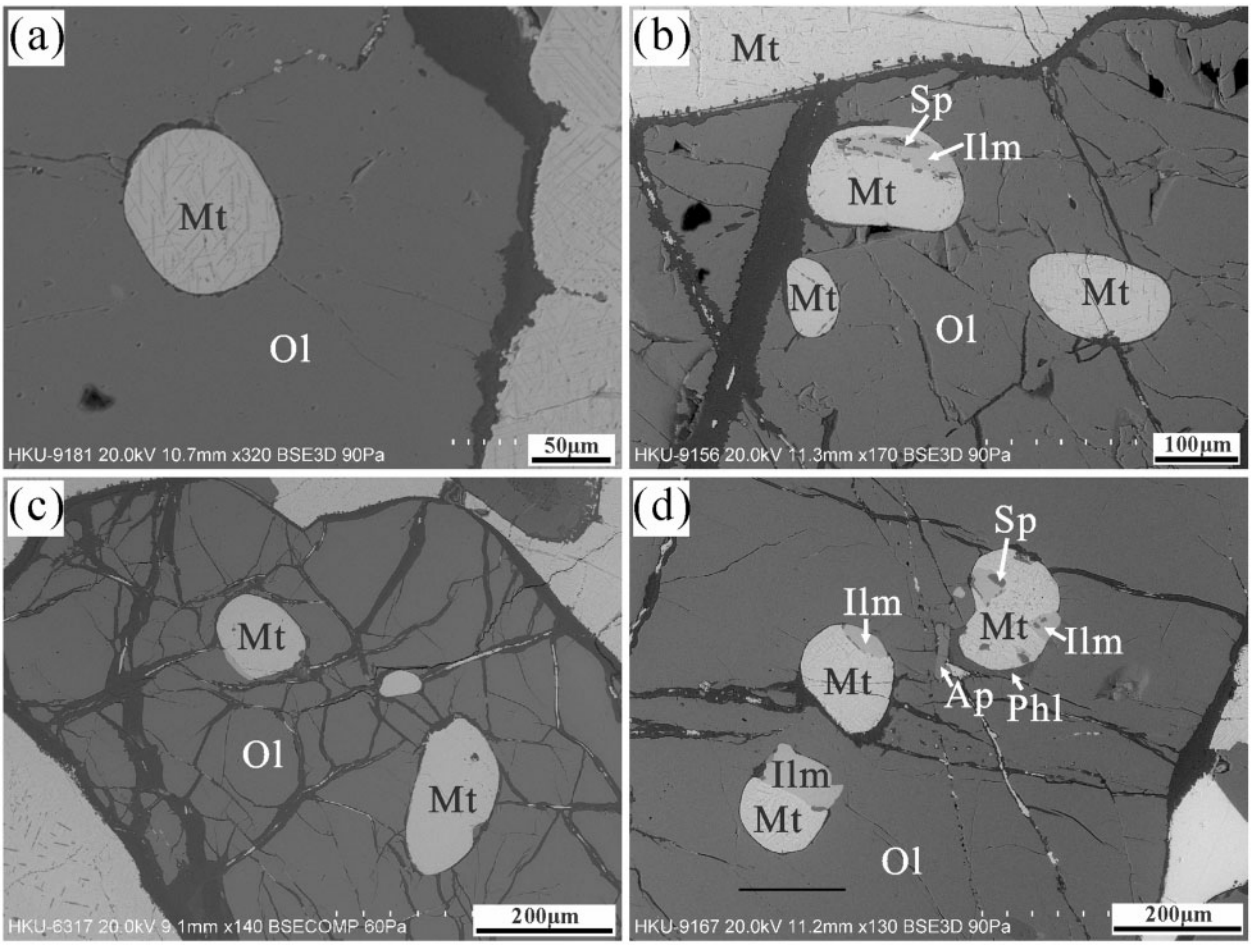

Fig. 6. Back-scattered electron images showing the occurrence of rounded to subrounded mineral inclusions composed of titanomagnetite (a) and (c) (samples BM11-171 and BM11-37, respectively) or titanomagnetite–ilmenite–spinel (b) and (d) (samples BM11-87 and BM11-171, respectively) hosted in cumulus olivine in the oxide ores of the Lower Zone of the Baima intrusion. Apatite and phlogopite occasionally occur close to the inclusions (d). Ap, apatite; Phl, phlogopite; Ol, olivine; Mt, titanomagnetite; Ilm, ilmenite; Sp, spinel.

titanomagnetite of the oxide ores, but is slightly different from that in the gabbro (Fig. 10; Supplementary Data Table 1). LA-ICP-MS data for titanomagnetite in interstitial networks and in inclusions from net-textured and disseminated ores show roughly consistent amounts of TiO_2 (4·53–16·5 wt %), Al_2O_3 (2·02–3·97 wt %), MgO (1·12–2·18 wt %), and V (2892–4850 ppm) compared with data obtained by electron microprobe (Table 2); however, the data are less variable owing to the large spot size, so that average compositions of titanomagnetite including ilmenite and spinel exsolution lamellae were obtained. In terms of trace elements, Co (84·6–217 ppm), Zn (138–590 ppm), Ni (74·1–312 ppm) and Cr (74·2–668 ppm) contents are high, whereas Sc, Cu, Ga, Sr, Y, Zr, Nb, Mo, Sn, Ba, Hf and Ta are present in trace amounts. Rare earth element (REE) contents of the titanomagnetite are typically below or close to the detection limit. To compare the trace element contents of titanomagnetite in interstitial networks and inclusions, we have plotted multi-element variation diagrams for lithophile and chalcophile elements separately (Fig. 11). Compositions were normalized to abundances in CI chondrites (McDonough & Sun, 1995). The order of the elements plotted is based on the relative compatibility of each element in magnetite (see Dare *et al.*, 2012). The result shows that titanomagnetite in interstitial networks and inclusions has similar compositions of both lithophile and chalcophile elements. It is noteworthy that the strong depletion of Cr and more compatible chalcophile elements is consistent with early sulfide segregation (Zhang *et al.*, 2013) and early crystallization of chromite or Cr-rich titanomagnetite (Wang & Zhou, 2013; Zhou *et al.*, 2013).

Hornblende

Hornblende in the inclusions and on the rims of plagioclase and clinopyroxene in the oxide ores and gabbros is Ti-rich

Downloaded from https://academic.oup.com/petrology/article/55/5/951/1496553 by guest on 20 August 2022

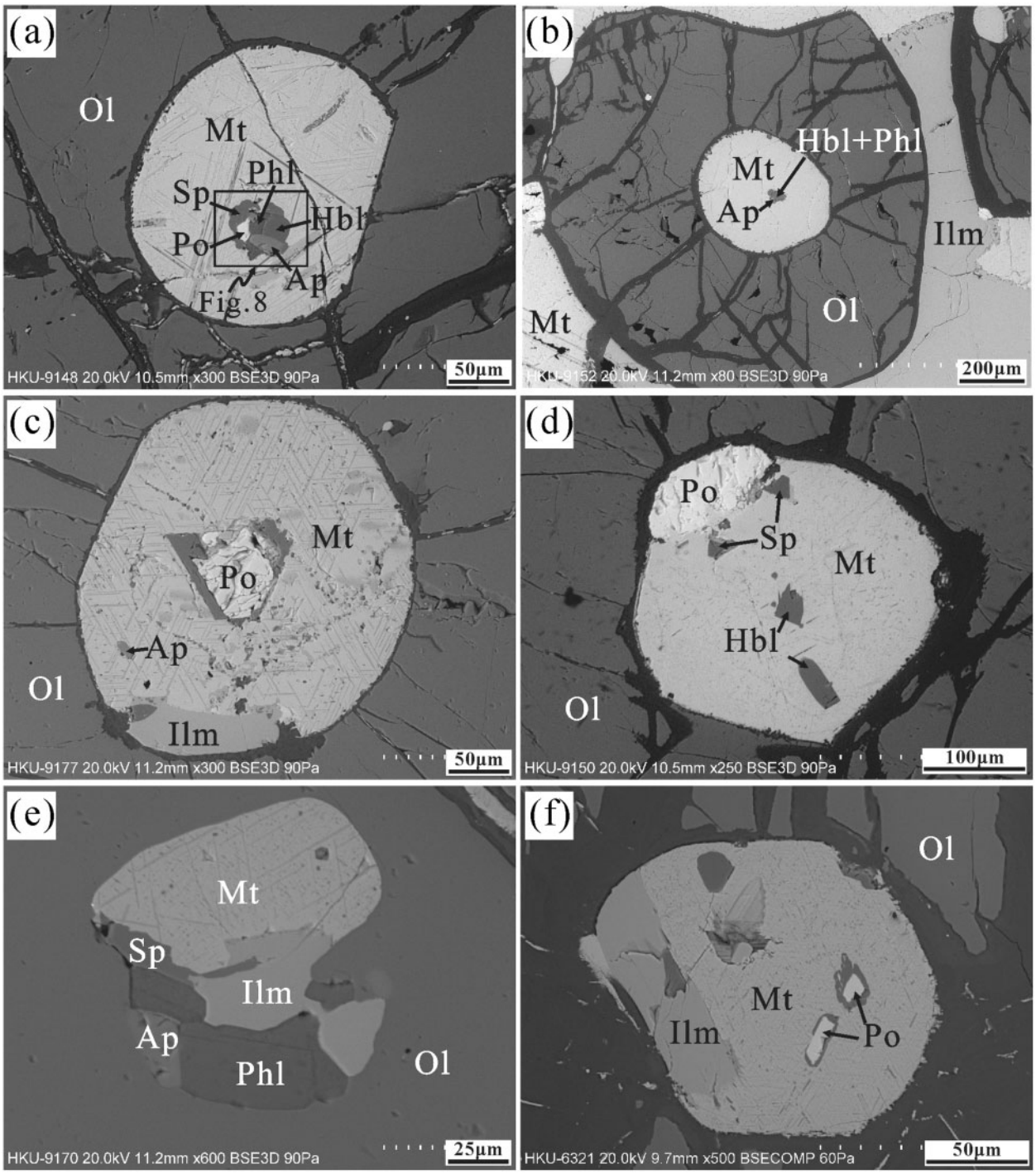

Fig. 7. Back-scattered electron images showing the mineral assemblages and their distribution in the multiphase solid inclusions in the oxide ores of the Lower Zone of the Baima intrusion. (a), (b) and (c) show zoned inclusions in olivine, showing the distribution of titanomagnetite (Mt) and/or ilmenite (Ilm) on the wall and phlogopite (Phl), spinel (Sp), hornblende (Hbl), pyrrhotite (Po) or apatite (Ap) in the centre [(a) and (b), sample BM11-87; (c) BM11-171]. (d), (e) and (f) Mineral assemblage of titanomagnetite, ilmenite, hornblende, spinel, phlogopite, apatite and pyrrhotite distributed randomly in the inclusions. Images of samples BM11-87, BM11-171 and BM11-37, respectively. The square in (a) shows the location of Fig. 8.

Downloaded from https://academic.oup.com/petrology/article/55/5/951/1496553 by guest on 20 August 2022

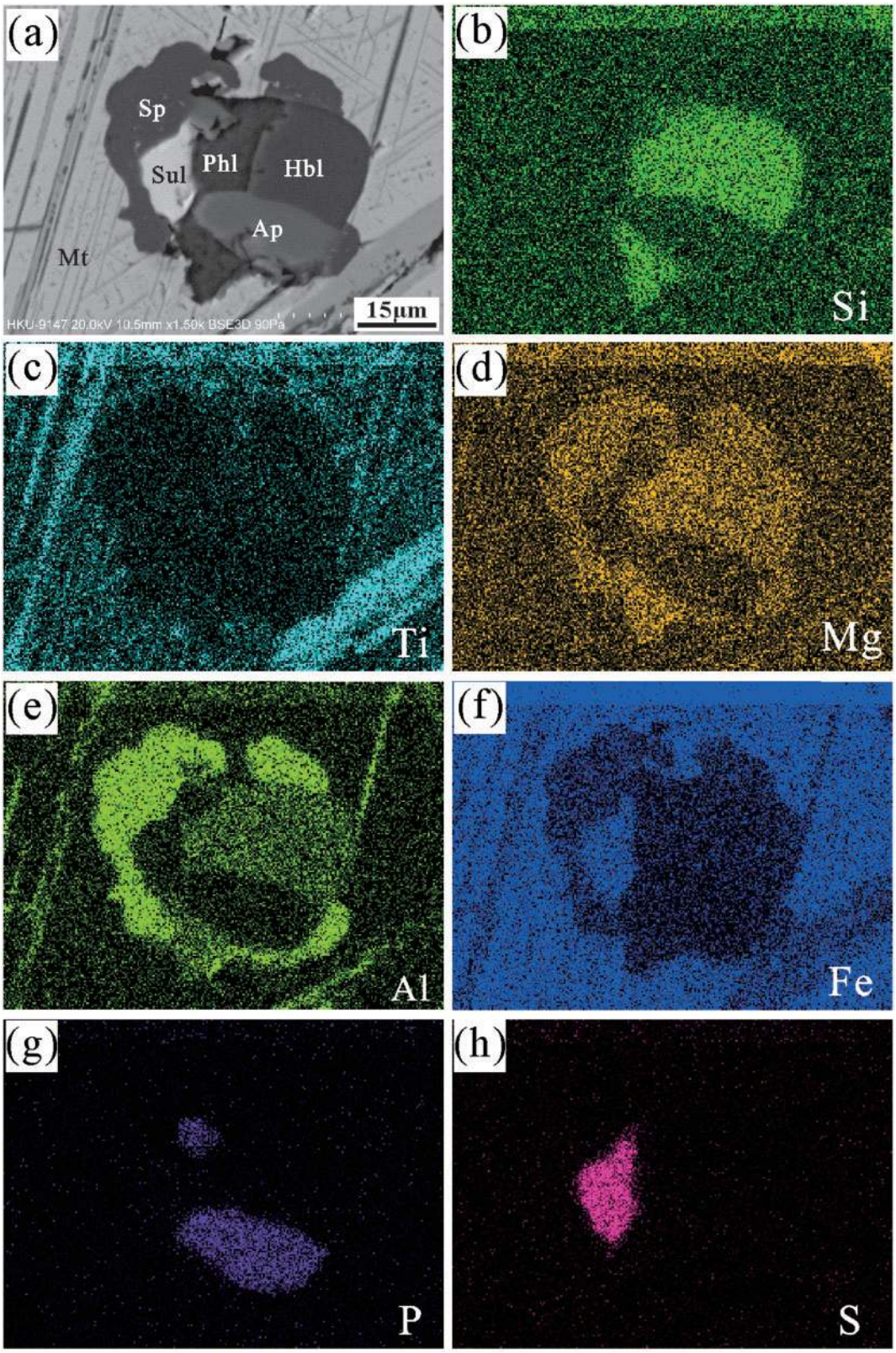

Fig. 8. BSE image (a) and element maps (b–h) of a typical zoned inclusion (Fig. 7a, sample BM11-87) showing that the daughter minerals in the inclusion have homogeneous compositions. Ap, apatite; phl, phlogopite; Hbl, hornblende; Mt, titanomanetite; Sp, spinel; Sul, sulfide.

Downloaded from https://academic.oup.com/petrology/article/55/5/951/1496553 by guest on 20 August 2022

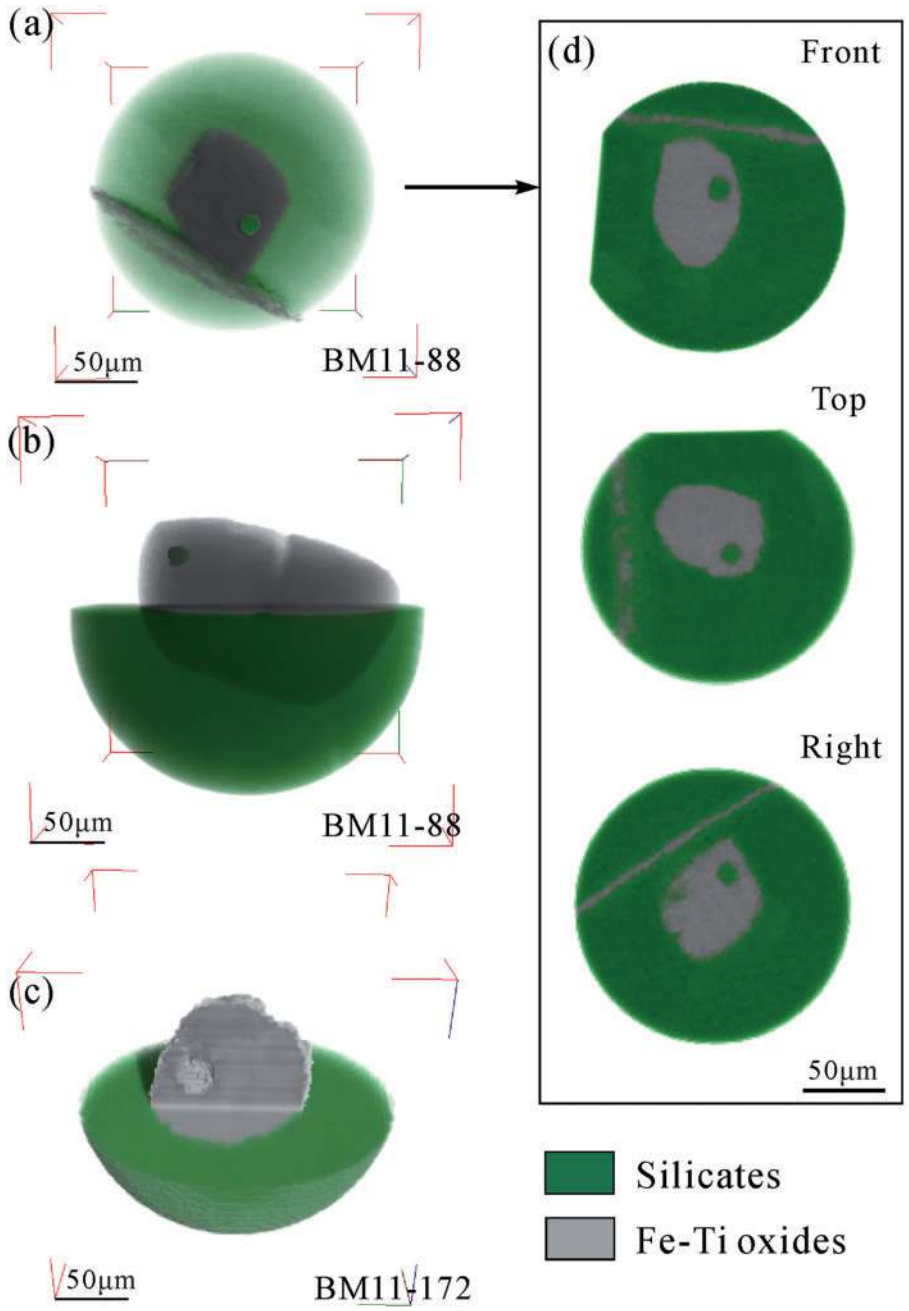

Fig. 9. Types of multiphase solid inclusions imaged by high-resolution X-ray computed tomography. (a) and (b) Subrounded inclusions composed of Fe–Ti oxides and silicates. The titanomagnetite is distributed in the outer zone and the silicates in the inner zone of the inclusions. (c) Rounded inclusion composed of Fe–Ti oxides and silicates. The silicates are connected with the host silicate wall instead of being trapped wholly in Fe–Ti oxides. (d) Front, top and right views of the 3-D image in (a), showing that the silicates in the inclusion are isolated from the host silicate wall.

magnesiohastingsite. Hornblende in the inclusions has slightly higher Mg# (70–77) and lower SiO_2 contents (38·0–41·4 wt %) than those of hornblende corona in both oxide ores and gabbros, which have similar Mg# ranging from 64 to 71 and SiO_2 contents from 40·0 to 42·4 wt % (Fig. 12, Table 3). Hornblende rims in the oxide ores have higher TiO_2 contents, ranging from 4·41 to 5·66 wt %, compared with hornblende rims in gabbro and those within the inclusions, which have similar TiO_2 contents varying from 2·5 to 4·5 wt %. Generally, hornblende in the inclusions has slightly higher Al_2O_3 than hornblende rims in the gabbro, whereas hornblende rims in the oxide ores have variable Al_2O_3 contents from 11·0 to 14·6 wt %.

Downloaded from https://academic.oup.com/petrology/article/55/5/951/1496553 by guest on 20 August 2022

Apatite, mica and sulfides

Apatite in mineral inclusions trapped in silicates contains 1·27–2·86 wt % F and 0·16–1·00 wt % Cl and is essentially fluorapatite. Minor elements in apatite include SiO_2, TiO_2, FeO, MgO and Al_2O_3 (Table 4). The composition of apatite is indicative of a magmatic origin, similar to that of the Panzhihua and Skaergaard intrusions (Nash, 1976; Pang *et al.*, 2009). The mica in the mineral inclusions is phlogopite with Mg# ranging from 79·4 to 85·8 wt %. It has low SiO_2 (36·6–37·8 wt %) and FeO (7·09–8·67 wt %) but high MgO (18·7–21·2 wt %) and TiO_2 (2·13–4·89 wt %) (Table 4). Sulfides in the inclusions are essentially pyrrhotite that contains chiefly Fe and S with <1 wt % Ni, Cu and Co.

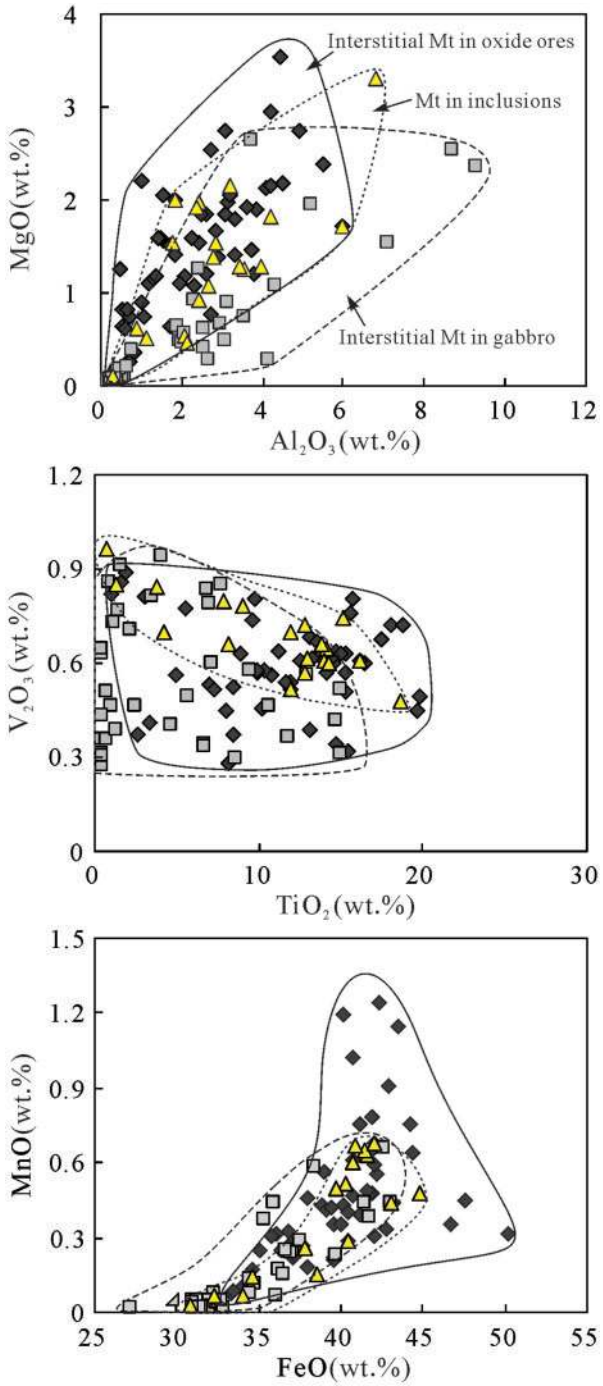

Fig. 10. Variation of MgO vs Al_2O_3 (wt %), V_2O_3 vs TiO_2 (wt %) and MnO vs FeO (wt %) for interstitial titanomagnetite (Mt) in oxide ores (diamonds), interstitial titanomagnetite in gabbros (squares) and titanomagnetite as a daughter mineral in inclusions (triangles).

DISCUSSION

Origin of multiphase solid inclusions

The multiphase solid inclusions identified in olivine grains can be explained as early crystallized liquidus mineral aggregates enclosed in coexisting olivine or as the crystallization products of trapped liquids in the silicates. The inclusions contain a mineral assemblage of titanomagnetite, ilmenite, hornblende, phlogopite, apatite and pyrrhotite; phlogopite and hornblende, in particular, are unlikely to crystallize before the cumulus silicate hosts in ferrobasaltic magmas based on Bowen's reaction series (Bowen, 1922). If the titanomagnetite in the inclusions had crystallized earlier than olivine, it would be rich in Cr, because of the high partition coefficient of Cr in magnetite ($D_{Cr}^{magnetite/melt} = 100–600$; see McCarthy *et al.*, 1985). However, none of the titanomagnetite grains in the inclusions have Cr contents comparable with those of early crystallized chromite and Cr-rich magnetite in the Xinjie and Hongge intrusions in the same region (Wang & Zhou, 2013). Thus, the interpretation of the inclusions as earlier mineral aggregates can be ruled out.

It is well documented that multiphase inclusions in minerals of igneous or metamorphic bodies are the crystallization products of trapped liquids or fluids during the crystallization of the host minerals (e.g. Loferski & Arculus, 1993; Hwang *et al.*, 2001; Ferrando *et al.*, 2005; Sparks & Mavrogenes, 2005). These inclusions are usually tens to hundreds of microns across. They may be rounded, elongated or irregular in shape and are composed of anhedral daughter minerals. There might be some minor unique mineral phases that are not present in the host rocks. Daughter minerals in the inclusions may not have compositions the same as those in the host rocks. Multiphase mineral inclusions within the olivine grains of the Baima intrusion have features identical to those reported previously, and can be interpreted as trapped melts in the growing olivine grains. The zonal distribution of minerals in the inclusions, characterized by titanomagnetite on the margins and other daughter minerals in the center, further indicates a crystallization sequence of titanomagnetite first from a trapped melt droplet, followed

Downloaded from https://academic.oup.com/petrology/article/55/5/951/1496553 by guest on 20 August 2022

by hornblende, apatite, phlogopite and pyrrhotite, probably saturated from the residual liquid.

The multiphase solid inclusions are dominated by titanomagnetite and ilmenite with minor hornblende, apatite, phlogopite and pyrrhotite, indicating that the trapped melts were extremely Fe–Ti-enriched, with small but significant amounts of P, S, F and H_2O. Using mineral modes obtained from 3-D image analysis and the compositions of the daughter minerals in multiphase solid inclusions within net-textured ore samples from the Baima intrusion (Fig. 8), the average composition of the melt inclusions is estimated to be 82–60 wt % FeO^T, 11·4–18·5 wt % TiO_2, 2·69–6·12 wt % Al_2O_3, 1·40–4·47 wt % MgO, 0·87–4·93 wt % SiO_2 and ~1 wt % volatiles including P, F, S and water (Table 5). Given the possibility that volatiles may escape during post-entrapment evolution of the

Table 2: Summary of LA-ICP-MS major and trace element compositions of titanomagnetite from the oxide ores of the Baima intrusion, SW China

Sample:	BM11-327		BM11-329		BM11-330		BM11-342		BM11-171	
Type:	diss.	incl.	net-text.	incl.	net-text.	incl.	diss.	incl.	net-text.	incl.
n:	5	6	6	5	7	9	4	6	5	5
Major element oxide (wt %)										
SiO_2	0·17	0·17	0·16	0·12	0·04	0·05	0·05	0·07	0·28	0·00
TiO_2	16·5	16·2	4·53	6·66	14·7	15·5	12·6	13·7	10·4	9·67
Al_2O_3	3·72	3·65	2·02	2·60	3·27	3·29	3·96	3·54	3·18	2·76
FeO^T	75·8	76·3	90·7	88·2	78·5	77·9	80·2	79·9	83·6	85·1
MnO	0·57	0·60	0·17	0·26	0·46	0·54	0·57	0·54	0·32	0·26
MgO	2·18	1·98	1·20	1·12	1·97	1·73	1·58	1·16	1·34	1·30
CaO	0·01	0·01	0·03	0·05	0·03	0·02	0·00	0·01	0·03	0·06
Na_2O	0·03	0·15	0·00	0·01	0·00	0·00	0·00	0·05	0·01	0·01
K_2O	0·00	0·00	0·00	0·01	0·01	0·00	0·00	0·00	0·03	0·03
Trace elements (ppm)										
Sc	13·9	15·7	7·29	8·09	13·1	13·1	14·6	11·7	7·74	6·46
Co	217	212	111	143	148	148	173	163	84·6	92·5
V	4442	4332	4850	4437	3634	4150	4793	4804	2892	3438
Cr	195	173	464	517	395	473	668	633	74·2	87·3
Ni	234	206	312	277	210	206	273	262	74·1	78·3
Cu	1·93	1·72	5·26	3·97	7·58	12·5	17·1	30·5	7·14	5·65
Zn	467	446	138	342	364	440	443	434	291	411
Ga	47·4	45·2	50·4	48·1	40·5	47·1	56·7	56·2	28·7	32·7
Rb	0·00	0·03	0·10	0·07	0·06	0·09	0·05	0·04	0·08	0·11
Sr	0·13	0·34	0·81	0·95	1·60	0·68	0·01	1·14	2·51	2·47
Y	0·06	0·08	0·06	0·07	0·12	0·05	0·00	0·09	0·19	0·22
Zr	7·07	7·03	2·88	6·52	6·21	10·3	4·77	6·21	6·35	8·70
Nb	1·14	0·94	0·01	0·29	0·76	1·77	0·46	1·20	0·07	0·18
Mo	0·63	0·75	0·32	1·12	0·62	0·61	0·05	0·36	0·80	1·06
Cd	0·20	0·43	0·00	0·06	0·06	0·25	0·35	0·16	0·04	0·06
Sn	1·19	1·32	1·47	2·10	1·56	1·91	2·89	2·45	1·23	1·77
Ba	0·08	0·19	0·11	0·18	0·05	0·10	0·03	0·29	0·02	0·04
Hf	0·24	0·30	0·03	0·20	0·25	0·43	0·25	0·43	0·11	0·25
Ta	0·08	0·08	0·03	0·02	0·05	0·12	0·03	0·05	0·11	0·24
W	0·00	0·02	0·00	0·04	0·01	0·02	0·01	0·02	0·00	0·02
Th	0·00	0·00	0·00	0·13	0·00	0·01	0·06	0·01	0·00	0·01
U	0·00	0·01	0·00	0·11	0·00	0·03	0·00	0·00	0·00	0·00

(continued)

Downloaded from https://academic.oup.com/petrology/article/55/5/951/1496553 by guest on 20 August 2022

Table 2: Continued

Sample:	BM11-354		BM11-87		BM11-196	
Type:	net-text.	incl.	net-text.	incl.	net-text.	incl.
n:	7	7	4	8	3	8
Major element oxide (wt %)						
SiO_2	0·03	0·13	0·00	0·25	0·02	0·13
TiO_2	11·8	14·6	11·5	13·4	14·8	15·3
Al_2O_3	2·41	3·97	3·54	3·30	3·36	3·38
FeO^T	81·7	78·3	81·9	80·2	78·3	77·8
MnO	0·60	0·58	0·41	0·57	0·55	0·60
MgO	1·60	1·48	1·61	1·30	2·00	1·79
CaO	0·10	0·01	0·01	0·01	0·01	0·00
Na_2O	0·00	0·00	0·00	0·00	0·00	0·00
K_2O	0·00	0·00	0·00	0·00	0·00	0·00
Trace elements (ppm)						
Sc	10·0	11·5	10·2	11·3	16·2	14·7
Co	138	165	160	163	191	157
V	4405	4598	4613	4192	4427	4451
Cr	172	230	174	172	189	192
Ni	144	160	145	171	226	189
Cu	14·9	6·60	19·9	4·0	7·41	4·51
Zn	368	590	463	555	366	406
Ga	46·9	50·2	56·5	47·8	48·1	49·4
Rb	0·20	0·00	0·07	0·02	0·00	0·05
Sr	0·74	0·18	0·64	0·94	0·09	0·06
Y	0·44	0·01	0·08	0·02	0·00	0·02
Zr	11·0	7·61	4·82	5·07	6·53	7·86
Nb	0·45	1·69	0·28	0·59	0·85	1·37
Mo	1·49	0·34	0·39	0·33	0·08	0·21
Cd	0·61	0·39	0·20	0·06	0·49	0·28
Sn	1·85	2·37	2·10	1·88	1·74	1·42
Ba	0·70	0·64	0·13	0·27	0·00	0·13
Hf	0·12	0·27	0·11	0·29	0·31	0·45
Ta	0·03	0·11	0·03	0·05	0·02	0·10
W	0·03	0·01	0·01	0·00	0·01	0·02
Th	0·00	0·00	0·00	0·00	0·02	0·00
U	0·00	0·02	0·00	0·01	0·00	0·00

diss, disseminated; incl, inclusion; net-text., net-textured.

Fe–Ti-rich droplets (Kent, 2008), the trapped melts may have contained even more volatiles.

Trapped liquids within silicate minerals may record the compositional evolution of the host magmas. In the Baima intrusion, olivine grains hosting multiphase solid inclusions occur in the Lower Zone. If fractional crystallization is the sole process responsible for melt evolution, the magma composition at this stage is more probably ferrobasaltic, slightly evolved compared with the Baima parental magma. However, the liquids inferred from the multiphase solid inclusions with extremely high FeO^T and TiO_2 and low SiO_2 do not resemble any known silicate magmas, and are different from the product of fractional crystallization (e.g. Toplis & Carroll, 1996; Namur *et al.*, 2012; VanTongeren & Mathez, 2012). In contrast, the Fe–Ti oxide-rich multiphase inclusions could have formed from

Downloaded from https://academic.oup.com/petrology/article/55/5/951/1496553 by guest on 20 August 2022

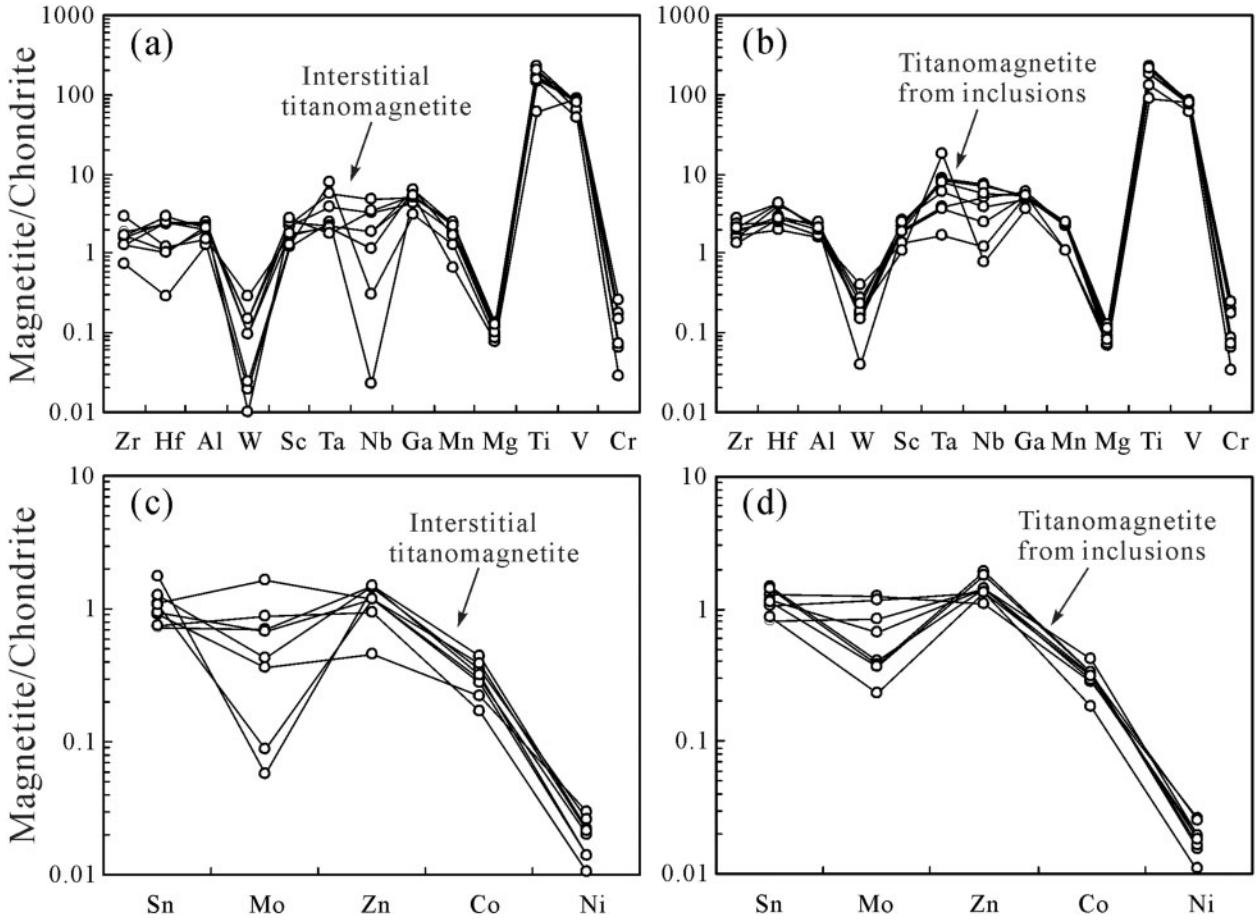

Fig. 11. Normalized multi-element variation patterns for lithophile elements (a, b) and chalcophile elements (c, d) in interstitial titanomagnetite and titanomagnetite from inclusions. Normalized to CI carbonaceous chondrites using values from McDonough & Sun (1995).

trapped Fe–Ti-rich melts that immiscibly separated from the ferrobasaltic magmas. Although such extremely Fe–Ti-rich mineral inclusions have not previously been reported in the literature, spherical inclusions consisting dominantly of sulfides are commonly observed (Naldrett, 1999; Holwell *et al.*, 2011; Park *et al.*, 2013). These sulfide inclusions are also multiphase and consist of a variety of sulfide minerals including pyrrhotite, pyrite, and chalcopyrite and Fe-oxides. They have been considered to have formed from melt droplets immiscible in mafic magmas. We speculate that the spherical multiphase solid inclusions in the Baima intrusion formed from small globules of immiscible Fe–Ti-rich melt that segregated from ferrobasaltic magma. These immiscible Fe–Ti-rich droplets were preferentially trapped in the crystallizing olivine grains and remained rounded with cooling and crystallization. The estimated compositions of the Fe–Ti-rich liquids may extend the compositions of Fe–Ti–Ca–P-rich melts to a more Fe–Ti enriched end-member compared with those with up to 80 wt % $FeO + TiO_2 + MgO + CaO + P_2O_5$ reported by Kamenetsky *et al.* (2013) for immiscible melt pools in tholeiitic gabbros in the Siberian large igneous province.

Origin of the Baima Fe–Ti–(V) oxide deposit

The Baima intrusion hosts the second largest Fe–Ti–(V) oxide deposit in the Panxi region. The origin of such giant deposits remains a matter of debate (Zhou *et al.*, 2005, 2013; Pang *et al.*, 2008*b*, 2009; Howarth *et al.*, 2013; Song *et al.*, 2013). The main concern centers on whether Fe–Ti oxides are crystallized from the same silicate magma as the silicate minerals, or alternatively, from Fe–Ti-rich melts immiscibly separated from silicate magmas.

Our understanding of the origin of multiphase solid inclusions in the Baima intrusion has important implications for the formation of the giant ore deposits. To determine whether or not the interstitial titanomagnetite in net-textured oxide ores has formed from immiscible Fe-Ti-rich melts, like the inclusions, we compare the compositions of titanomagnetite in the inclusions and in the interstitial network. The compositional comparison shows that the

Downloaded from https://academic.oup.com/petrology/article/55/5/951/1496553 by guest on 20 August 2022

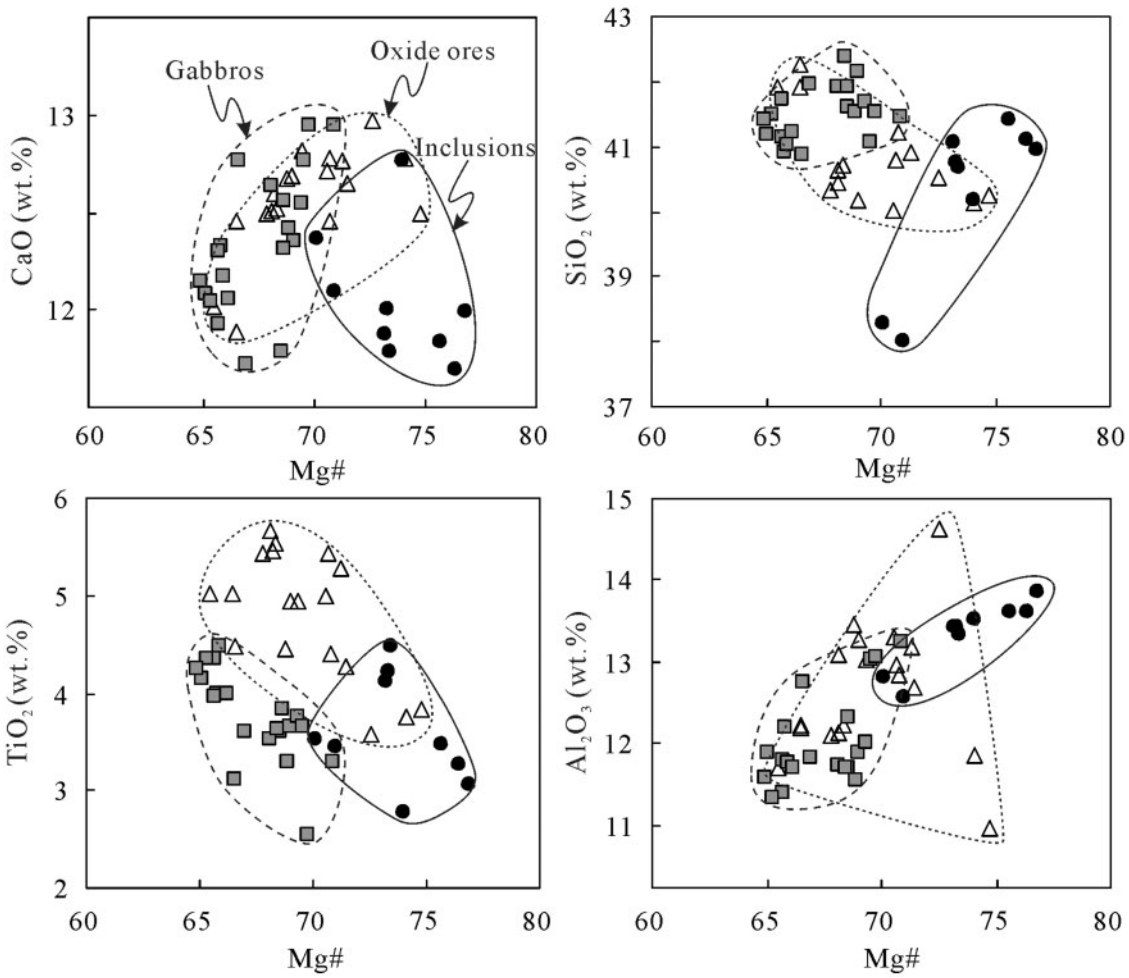

Fig. 12. Variation of CaO, SiO_2, TiO_2 and Al_2O_3 (wt %) contents of hornblende as a function of Mg# [Mg# = Mg/(Mg + Fe)]. Distinction is made between hornblende in inclusions (black circles), hornblende as rims in oxide ores (white triangles) and hornblende as rims in gabbro (grey squares).

titanomagnetite in the inclusions has compositions, in particular of compatible trace elements, identical to that of titanomagnetite in the interstitial network (Fig. 11). Net-textured oxide ore, in contrast, has olivine, clinopyroxene and plagioclase grains enclosed in a continuous network of Fe–Ti oxides. This structure is comparable with that of net-textured sulfide ores, which are considered to be formed from segregation and concentration of droplets of sulfide liquids from a silicate magma (e.g. Naldrett, 1999). We therefore propose that the interstitial Fe–Ti oxides of the Baima oxide ores were formed from compositionally similar Fe–Ti-rich liquids to those recorded in the multiphase solid inclusions. The composition of the immiscible Fe–Ti-rich liquids is nearly identical to Fe–Ti-rich melts that form massive and net-textured oxide ores in the Panzhihua intrusion proposed by Zhou *et al.* (2005).

Coexisting, immiscible melts during the formation of the Baima intrusion are consistent with some of its unique textural features that are difficult to explain by normal processes of fractional crystallization. Examples are texturally embayed plagioclase and clinopyroxene embedded in an interconnected Fe–Ti oxide network, and hornblende coronae at the contact of plagioclase and Fe–Ti oxides. Tepley *et al.* (1999) described similar rim and embayed textures of plagioclase phenocrysts from Chaos Crags, California and proposed that plagioclase crystallized from a silicic magma was partially resorbed and subsequently overgrown in a hybrid andesitic magma. Likewise, mantled feldspar has been used to suggest a magma mixing process (Hibbard, 1981). The formation of skeletal and dendritic olivine crystals require rapid supersaturation, which can be attributed to either a change of water content or adiabatic expansion of the magma (Donaldson, 1974), or unmixing of an Fe-rich magma induced by mutually enhanced solubilities of P and Fe in a silicate magma. Therefore, it can be inferred that presence

Downloaded from https://academic.oup.com/petrology/article/55/5/951/1496553 by guest on 20 August 2022

Table 3: Representative compositions of hornblende from the Baima intrusion

Sample:	BM11-45			BM11-48			BM11-49		BM11-54		BM11-57		BM11-68	BM11-87				BM11-171	
Point:	1	2	3	1	2	3	1	2	1	2	1	2	1	1	2	3	4	1	2
Hornblende rim in oxide ores																			
SiO_2	40·6	40·7	40·3	40·5	40·8	40·0	40·9	40·6	40·7	40·3	40·5	40·1	40·3	41·2	40·5	40·2	41·9	42·3	41·9
TiO_2	5·42	4·99	5·29	5·54	5·43	4·41	5·66	5·03	5·47	4·93	4·95	4·44	4·26	5·03	4·47	3·57	3·76	3·83	3·76
Al_2O_3	13·0	13·3	13·2	12·2	12·1	12·8	12·1	12·2	13·1	13·3	13·0	13·5	12·7	11·7	12·2	14·6	11·8	11·0	11·8
FeO	9·34	9·51	8·91	10·1	10·5	9·40	10·4	11·3	10·3	9·93	9·66	10·13	9·49	11·6	11·3	9·02	9·05	8·69	9·05
MnO	0·08	0·06	0·09	0·06	0·09	0·14	0·09	0·18	0·08	0·04	0·25	0·15	0·07	0·09	0·17	0·07	0·07	0·11	0·07
MgO	12·6	12·8	12·4	12·3	12·4	12·8	12·4	12·5	12·4	12·4	12·3	12·5	13·3	12·4	12·6	13·4	14·5	14·5	14·5
CaO	12·8	12·7	12·8	12·5	12·5	12·5	12·5	12·5	12·6	12·7	12·8	12·7	12·7	12·0	11·9	13·0	12·8	12·5	12·8
Na_2O	3·04	3·11	3·35	2·99	3·01	3·09	2·97	2·99	2·90	2·67	3·10	3·14	3·36	3·36	2·87	3·08	2·66	2·96	2·66
K_2O	1·07	1·11	1·00	1·31	1·28	1·04	1·48	1·44	1·52	1·54	1·20	1·20	0·82	1·04	1·15	1·09	1·28	1·19	1·28
F	0·09	0·10	0·08	0·10	0·08	—	—	—	0·12	0·08	—	—	—	—	—	—	—	—	—
Cl	0·02	0·01	0·02	0·04	0·05	—	—	—	0·03	0·02	—	—	—	—	—	—	—	—	—
Total	97·9	98·3	97·4	97·6	98·1	96·1	98·7	98·7	99·2	97·8	97·8	97·8	97·0	98·5	97·1	98·0	97·9	97·0	97·9
Si	5·98	5·97	5·96	6·01	6·03	6·00	6·02	6·00	5·95	5·96	5·99	5·94	5·99	6·09	6·05	5·89	6·15	6·25	6·15
Ti	0·60	0·55	0·59	0·62	0·60	0·50	0·63	0·56	0·60	0·55	0·55	0·49	0·48	0·56	0·50	0·39	0·42	0·43	0·42
Al	2·25	2·30	2·30	2·14	2·11	2·27	2·10	2·12	2·25	2·31	2·27	2·35	2·23	2·04	2·16	2·53	2·05	1·91	2·05
Fe^{2+}	1·15	1·17	1·10	1·26	1·29	1·18	1·28	1·39	1·26	1·23	1·19	1·25	1·18	1·44	1·41	1·11	1·11	1·07	1·11
Mn	0·01	0·01	0·01	0·01	0·01	0·02	0·01	0·02	0·01	0·01	0·03	0·02	0·01	0·01	0·02	0·01	0·01	0·01	0·01
Mg	2·76	2·80	2·73	2·72	2·73	2·85	2·73	2·76	2·71	2·73	2·70	2·76	2·95	2·72	2·80	2·93	3·17	3·18	3·17
Ca	2·02	2·00	2·02	1·99	1·98	2·00	1·97	1·97	1·97	2·01	2·03	2·01	2·02	1·90	1·91	2·04	2·01	1·98	2·01
Na	0·87	0·89	0·96	0·86	0·86	0·90	0·85	0·86	0·82	0·77	0·89	0·90	0·97	0·96	0·83	0·88	0·76	0·85	0·76
K	0·20	0·21	0·19	0·25	0·24	0·20	0·28	0·27	0·28	0·29	0·23	0·23	0·16	0·20	0·22	0·21	0·24	0·23	0·24
Total	15·8	15·9	15·9	15·9	15·9	15·9	15·9	15·9	15·9	15·9	15·9	16·0	16·0	15·9	15·9	16·0	15·9	15·9	15·9
Mg#	70·6	70·6	71·3	68·3	67·8	70·73	68·1	66·5	68·2	69·0	69·4	68·8	71·4	65·5	66·5	72·6	74·1	74·8	74·1

Sample:	BM11-79				BM11-85		BM11-93											BM11-160
Point:	1	2	3	4	1	2	1	2	3	4	5	6	7	8	9	10	11	1
Hornblende rim in (olivine) gabbro																		
SiO_2	41·6	41·9	42·4	42·0	41·5	41·1	42·2	41·5	41·7	40·9	41·2	41·0	41·2	41·2	41·7	41·5	41·4	41·9
TiO_2	3·61	3·51	3·63	3·60	3·29	3·66	3·66	3·29	3·75	3·99	3·95	4·48	3·98	4·14	4·34	4·34	4·24	3·82
Al_2O_3	12·3	11·7	11·7	11·8	13·2	13·0	11·9	11·5	12·0	12·2	11·8	11·8	11·7	11·9	11·4	11·3	11·6	11·7
FeO	10·8	10·9	10·9	11·4	10·2	10·4	10·7	10·5	10·4	11·3	11·6	11·7	11·5	11·9	11·8	11·7	12·1	10·8
MnO	0·16	0·07	0·07	0·11	0·12	0·10	0·15	0·08	0·13	0·14	0·17	0·16	0·18	0·12	0·20	0·12	0·17	0·09
MgO	13·3	13·1	13·3	12·9	13·9	13·4	13·4	13·0	13·2	12·2	12·5	12·7	12·6	12·5	12·6	12·3	12·5	13·3
CaO	12·6	12·6	11·8	11·7	13·0	12·8	12·4	12·4	12·5	12·3	12·3	12·2	12·1	12·1	11·9	12·0	12·2	12·3
Na_2O	2·66	2·63	2·49	2·58	2·58	2·52	2·66	2·55	2·77	2·55	2·68	2·69	2·94	2·71	2·85	2·72	2·79	2·55
K_2O	1·45	1·40	1·34	1·32	1·58	1·39	1·33	1·30	1·44	1·56	1·34	1·34	1·23	1·17	1·11	1·30	1·20	1·15
F	0·10	0·16	—	—	—	—	0·08	0·08	0·07	0·01	0·05	0·06	0·02	0·08	—	0·07	0·03	—
Cl	0·06	0·05	—	—	—	—	0·05	0·05	0·05	0·06	0·04	0·06	0·04	0·04	0·05	0·05	0·05	—
Total	98·5	97·9	97·5	97·4	99·3	98·4	98·3	96·2	97·9	97·1	97·4	98·1	97·4	97·7	97·9	97·4	98·1	97·7
Si	6·12	6·20	6·26	6·23	6·04	6·04	6·20	6·23	6·16	6·12	6·14	6·09	6·15	6·13	6·18	6·19	6·14	6·19
Ti	0·40	0·39	0·40	0·40	0·36	0·41	0·40	0·37	0·42	0·45	0·44	0·50	0·45	0·46	0·48	0·49	0·47	0·43
Al	2·14	2·05	2·04	2·07	2·27	2·26	2·06	2·04	2·09	2·15	2·07	2·06	2·06	2·09	1·99	1·99	2·02	2·04
Fe^{2+}	1·33	1·35	1·34	1·41	1·24	1·28	1·32	1·32	1·28	1·41	1·45	1·45	1·43	1·48	1·46	1·46	1·50	1·34
Mn	0·02	0·01	0·01	0·01	0·01	0·01	0·02	0·01	0·02	0·02	0·02	0·02	0·02	0·01	0·03	0·02	0·02	0·01
Mg	2·91	2·89	2·92	2·86	3·02	2·93	2·94	2·92	2·90	2·71	2·77	2·81	2·80	2·76	2·79	2·74	2·77	2·93
Ca	1·98	2·00	1·86	1·86	2·02	2·01	1·94	2·00	1·99	1·98	1·97	1·93	1·93	1·93	1·89	1·92	1·93	1·95
Na	0·76	0·76	0·71	0·74	0·73	0·72	0·76	0·74	0·79	0·74	0·78	0·78	0·85	0·78	0·82	0·79	0·80	0·73
K	0·27	0·27	0·25	0·25	0·29	0·26	0·25	0·25	0·27	0·30	0·26	0·25	0·23	0·22	0·21	0·25	0·23	0·22
Total	15·9	15·9	15·8	15·8	16·0	15·9	15·9	15·9	15·9	15·9	15·9	15·9	15·9	15·9	15·9	15·8	15·9	15·8
Mg#	68·6	68·1	68·5	67·0	70·9	69·6	69·1	68·9	69·4	65·8	65·7	65·9	66·2	65·1	65·7	65·3	64·9	68·6

(continued)

Downloaded from https://academic.oup.com/petrology/article/55/5/951/1496553 by guest on 20 August 2022

Table 3: Continued

Sample:	BM11-361		BM11-87								
Point:	1	2	1	2	3	4	5	6	7	8	9
Hornblende in the inclusions of the oxide ores											
SiO_2	40·9	41·5	40·2	38·3	38·0	41·1	40·7	40·7	41·4	40·9	41·1
TiO_2	3·12	2·54	2·79	3·52	3·44	4·12	4·22	4·47	3·48	3·07	3·25
Al_2O_3	12·8	13·1	13·5	12·8	12·6	13·4	13·4	13·3	13·6	13·8	13·6
FeO	11·6	10·5	8·79	12	11	9·53	9·44	9·59	8·57	8·75	8·74
MnO	0·09	0·10	0·11	0·06	0·09	0·09	0·11	0·08	0·06	0·07	0·11
MgO	13·0	13·7	14·1	12·9	12·9	14·2	14·2	14·1	14·5	14·8	14·6
CaO	12·8	12·9	12·8	12·4	12·1	11·9	12·0	11·8	11·8	12·0	11·7
Na_2O	2·25	2·25	2·47	2·96	2·86	3·05	2·75	2·75	2·70	2·74	2·62
K_2O	1·49	1·39	1·73	1·46	1·60	0·92	1·20	1·25	1·43	1·39	1·60
F	—	—	—	—	—	—	—	—	—	—	—
Cl	—	—	—	—	—	—	—	—	—	—	—
Total	98·0	97·9	96·4	96·3	94·9	98·2	98·1	98·1	97·6	97·6	97·3
Si	6·07	6·12	6·00	5·80	5·84	5·99	5·97	5·96	6·05	5·99	6·03
Ti	0·35	0·28	0·31	0·40	0·40	0·45	0·47	0·49	0·38	0·34	0·36
Al	2·23	2·27	2·38	2·29	2·28	2·31	2·32	2·30	2·35	2·39	2·35
Fe^{2+}	1·45	1·30	1·10	1·24	1·21	1·13	1·13	1·12	1·02	0·97	0·99
Mn	0·01	0·01	0·01	0·01	0·01	0·01	0·01	0·01	0·01	0·01	0·01
Mg	2·88	3·00	3·13	2·91	2·95	3·08	3·09	3·08	3·17	3·23	3·19
Ca	2·03	2·04	2·04	2·01	1·99	1·86	1·88	1·85	1·86	1·88	1·84
Na	0·65	0·64	0·72	0·87	0·85	0·86	0·78	0·78	0·77	0·78	0·75
K	0·28	0·26	0·33	0·28	0·31	0·17	0·22	0·23	0·27	0·26	0·30
Total	15·9	15·9	16·02	16·19	16·17	15·92	15·91	15·90	15·90	15·98	15·94
Mg#	66·6	69·8	74·0	70·2	71·0	73·2	73·3	73·5	75·6	76·8	76·4

of water or unmixing processes are essential to account for the formation of plagioclase rims and the embayed textures of olivine, plagioclase and clinopyroxene in the Baima intrusion. Howarth *et al.* (2013) proposed a model involving multiple replenishments of magma with variable H_2O content, titanomagnetite crystal load and volume that were in disequilibrium with the entrained silicates. However, if titanomagnetite was crystallized before magma emplacement, it would be unlikely to be carried within the magmas because of its high density (5·15 g cm^{-3}). We suggest that immiscible Fe–Ti oxide melts that contained a small, but significant, amount of water produced the embayed and rimmed textures in the Baima intrusion.

Considering that the net-textured Fe–Ti oxide ores make up the majority of the ores in the Baima intrusion, an immiscible origin for them allows us to propose a genetic model for the formation of the giant deposit in the Baima intrusion (Fig. 13). The parental magma of the Baima intrusion, rich in Fe and Ti, underwent fractionation at depth before being emplaced into a shallow-level magma chamber (Zhang *et al.*, 2012, 2013; Zhou *et al.*, 2013). Plagioclase and olivine began to crystallize during cooling of the magma. Olivine tended to settle at the base of the magma chamber whereas a considerable amount of plagioclase floated upwards (Fig. 13a). Continuous fractionation of plagioclase and olivine promoted enrichment of Fe and Ti in the residual silicate magma and subsequently resulted in the unmixing of an Fe–Ti-rich melt from the silicate magma. The dense Fe–Ti-rich melt droplets with low viscosity tended to sink to the bottom of the chamber where they infiltrated downwards through the unconsolidated crystal pile and filled in the interstitial spaces between the silicate minerals, forming the net-textured and disseminated ores (Fig. 13b). In some areas, small droplets of such immiscible Fe–Ti-rich melt were trapped in the growing silicate crystals and crystallized titanomagnetite, ilmenite, apatite, phlogopite, hornblende and pyrrhotite

Downloaded from https://academic.oup.com/petrology/article/55/5/951/1496553 by guest on 20 August 2022

Table 4: Representative analyses of phlogopite and apatite from the multiphase solid inclusions enclosed in cumulus silicates of oxide ores in the Baima intrusion

Mineral:	phlogopite												apatite						
Sample:	BM11-87								BM11-171				BM11-87					BM11-171	
Point:	1	2	3	4	5	6	7	8	1	2	3	4	1	2	3	4	5	1	2
SiO_2	37·5	37·0	37·4	37·1	36·6	37·4	37·4	37·7	36·7	37·1	37·8	36·7	0·11	0·05	0·59	0·08	0·33	0·13	0·44
TiO_2	3·76	4·13	2·48	3·32	2·67	4·89	3·59	3·50	3·95	2·35	3·07	2·13	0·08	0·28	0·25	0·02	0·23	0·07	0·03
Al_2O_3	16·7	16·3	17·3	16·6	17·2	16·2	16·6	16·4	16·7	17·2	16·7	16·3	0·03	0·13	0·51	0·00	0·29	0·01	0·09
FeO	8·18	8·67	7·74	8·13	7·09	8·08	7·56	7·49	8·33	7·42	7·32	7·44	0·71	2·26	1·39	0·17	1·27	0·52	0·57
MnO	0·01	0·08	0·06	0·04	0·03	0·01	0·03	0·01	0·04	0·02	0·01	0·05	0·03	0·02	0·04	0·00	0·00	0·05	0·02
MgO	19·5	18·7	20·4	20·3	20·5	18·8	19·7	19·9	20·0	21·2	20·5	19·9	0·01	0·06	0·41	0·06	0·18	0·02	0·40
CaO	0·02	—	0·08	0·00	1·41	0·00	0·00	0·02	—	0·04	0·02	0·17	55·2	56·1	52·6	52·7	52·5	54·5	53·1
Na_2O	0·64	0·58	0·33	0·52	0·61	0·57	0·66	0·71	0·47	0·38	0·64	0·63	—	—	—	—	—	—	—
K_2O	9·88	10·24	10·25	9·70	7·93	9·24	9·24	9·23	9·94	10·13	9·18	9·18	—	—	—	—	—	—	—
P_2O_5	—	—	—	—	—	—	—	—	—	—	—	—	42·5	40·5	41·0	41·9	41·6	42·8	42·2
F	—	—	—	—	—	—	—	—	—	—	—	—	2·86	n.a.	1·42	1·27	1·68	2·51	1·99
Cl	—	—	—	—	—	—	—	—	—	—	—	—	0·18	0·16	0·18	0·93	0·25	0·81	1·00
Total	96·1	95·7	96·0	95·7	94·0	95·1	94·8	95·0	96·0	95·7	95·2	92·5	101·7	99·6	98·4	97·1	98·3	101·5	99·8
Si	2·70	2·69	2·68	2·67	2·65	2·71	2·71	2·72	2·64	2·66	2·71	2·72	0·02	0·01	0·10	0·01	0·06	0·02	0·07
Ti	0·20	0·23	0·13	0·18	0·15	0·27	0·20	0·19	0·21	0·13	0·17	0·12	0·01	0·04	0·03	0·00	0·03	0·01	0·00
Al	1·41	1·40	1·46	1·41	1·47	1·38	1·41	1·39	1·41	1·45	1·41	1·42	0·00	0·01	0·05	0·00	0·03	0·00	0·01
Fe^{3+}	0·00	0·00	0·07	0·07	0·06	0·00	0·04	0·03	0·08	0·07	0·07	0·07	0·00	0·00	0·00	0·00	0·00	0·00	0·00
Fe^{2+}	0·49	0·53	0·40	0·42	0·37	0·49	0·42	0·42	0·43	0·38	0·37	0·39	0·10	0·31	0·19	0·02	0·18	0·07	0·08
Mn	0·00	0·01	0·00	0·00	0·00	0·00	0·00	0·00	0·00	0·00	0·00	0·00	0·00	0·00	0·00	0·00	0·00	0·00	0·00
Mg	2·09	2·03	2·18	2·18	2·21	2·03	2·13	2·14	2·14	2·27	2·19	2·20	0·00	0·01	0·10	0·01	0·05	0·00	0·10
Ca	0·00	0·00	0·01	0·00	0·11	0·00	0·00	0·00	0·00	0·00	0·00	0·01	9·87	10·03	9·41	9·42	9·38	9·74	9·49
Na	0·09	0·08	0·05	0·07	0·09	0·08	0·09	0·10	0·07	0·05	0·09	0·09	—	—	—	—	—	—	—
K	0·91	0·95	0·94	0·89	0·73	0·85	0·85	0·85	0·91	0·93	0·84	0·87	—	—	—	—	—	—	—
P	—	—	—	—	—	—	—	—	—	—	—	—	5·99	5·71	5·78	5·90	5·87	6·04	5·94
Total	7·89	7·90	7·91	7·89	7·84	7·80	7·85	7·85	7·89	7·94	7·85	7·90	15·99	16·12	15·67	15·38	15·58	15·89	15·70

(Fig. 13c). This model is comparable with those proposed for the net-textured ores in the Middle and Upper Zones of the Hongge intrusion (Wang & Zhou, 2013), the massive ores in the Lower Zone of the Panzhihua intrusion (Zhou *et al.*, 2005, 2013) and the net-textured ores in the Upper Zone of the Bushveld Complex (Von Gruenewaldt, 1993).

Significance of immiscible Fe–Ti-rich melts in layered intrusions

Differentiation of tholeiitic basaltic magma has been one of the oldest controversies in igneous petrology (e.g. Bowen, 1928; Wager & Brown, 1968), particularly the nature of the magmas from which extensive Fe–Ti oxides crystallize (Lister, 1966; Philpotts, 1967; Kolker, 1982). Layered mafic intrusions provide evidence for the existence of Fe-rich and Si-rich liquids produced by extreme crystal fractionation of mafic magmas (Jakobsen *et al.*, 2005, 2011; Charlier *et al.*, 2011). This has been verified by laboratory experiments showing that immiscibility can occur in highly evolved tholeiitic basaltic magmas after 90–95% crystallization (Dixon & Rutherford, 1979; Naslund, 1983). The Fe-rich melts commonly contain 18–32 wt % FeO^T and 30–50 wt % SiO_2, and the Si-rich counterpart has 4–12 wt % FeO^T and 60–76 wt % SiO_2 (Charlier & Grove, 2012). The segregation of two liquids is a possible explanation for the presence of temporally and spatially related granitic and ferrobasaltic rocks on an outcrop scale (Jakobsen *et al.*, 2005; Charlier *et al.*, 2011). In contrast, the immiscible Fe–Ti-rich melts recorded in the Baima

Downloaded from https://academic.oup.com/petrology/article/55/5/951/1496553 by guest on 20 August 2022

Table 5: Reconstructed compositions of Fe–Ti-rich melts in the Lower Zone of the Baima intrusion

	Mt*	Ilm	Hbl	Phl	Ap	Sp	Estimated melt composition 1(wt %)†	Estimated melt composition 2(wt %)†
SiO_2	0·65	0·00	40·2	37·4	0·11	0·10	0·78	4·93
TiO_2	11·5	53·0	2·79	2·48	0·08	0·29	11·5	18·5
Al_2O_3	2·49	0·01	13·5	17·3	0·03	62·8	2·62	6·12
FeO^T	82·8	43·0	8·79	7·74	0·71	21·2	82·4	59·6
MnO	0·40	1·10	0·11	0·06	0·03	0·33	0·40	0·50
MgO	1·28	3·04	14·1	20·4	0·01	14·4	1·35	4·47
CaO	0·00	0·00	12·8	0·08	55·2	0·00	0·09	2·00
Na_2O	0·01	0·00	2·47	0·33	0·00	0·07	0·01	0·05
K_2O	0·00	0·00	1·73	10·2	0·00	0·01	0·02	1·25
P_2O_5	0·00	0·00	0·00	0·00	42·46	0·00	0·05	1·53
Total	99·1	100·2	96·4	96·0	98·6	99·2	99·1	99·0
vol % 1‡	99	0	0·3	0·3	0·2	0·2		
vol % 2‡	50	20	0	20	5	5		
D§	5·2	4·8	3·2	2·7	3·2	3·6		

Ap, apatite; Hbl, hornblende; Ilm, ilmenite; Mt, titanomagnetite; Phl, phlogopite; Sp, spinel.
*Composition of titanomagnetite was obtained from *in situ* LA-ICP-MS analyses.
†Melt compositions 1 and 2 correspond to estimated volume percentage of 1 and 2, respectively.
‡Volume percentage of the daughter minerals were estimated in a 3-D view according to typical inclusions of Fig. 7a and e, which contain the lowest and highest percentage of silicates, respectively.
§Densities (*D*) are estimated from values given by Deer *et al*. (1992).

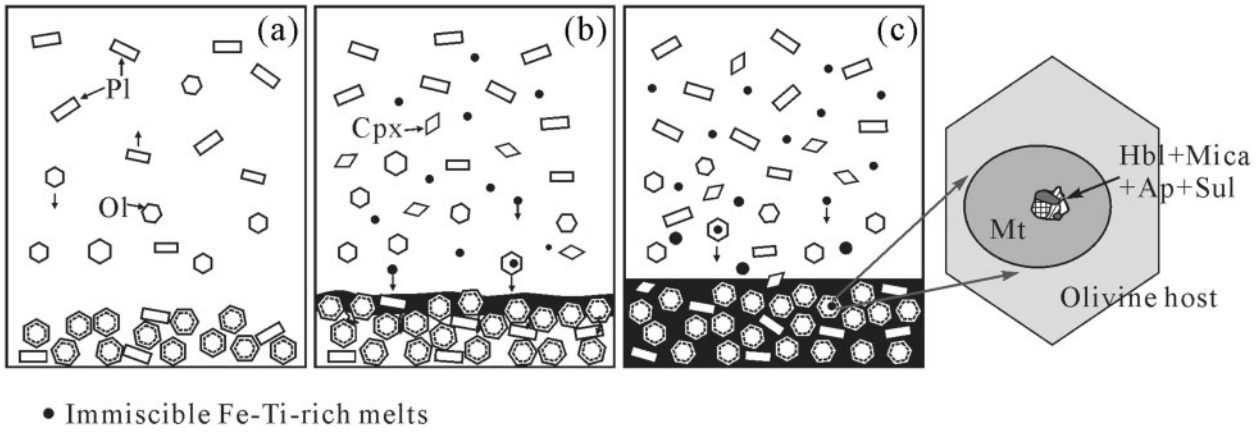

Fig. 13. Model for the formation of Fe–Ti oxide ores in the Baima intrusion. (a) With falling temperature, plagioclase and olivine begin to crystallize. Olivine sinks to the floor of the magma chamber whereas a considerable amount of plagioclase floats upward. The residual magma becomes denser and more enriched in Fe and Ti. (b) The immiscible separation of Fe–Ti-rich melt droplets occurs possibly owing to the high Fe and Ti melt content and the presence of water, P, S and F. Small droplets of segregated Fe–Ti-rich liquid are trapped in the growing silicate crystals or settle onto the cumulus silicates at the floor. (c) The low-viscosity, high-density, volatile-bearing, immiscible, Fe–Ti-rich melt accumulates above the cumulus crystals and percolates down through the unconsolidated crystal pile, filling in the interstitial spaces in the silicate crystal framework. In this scenario, Fe–Ti oxides crystallize from the Fe–Ti-rich liquid, forming an interconnected network enclosing cumulus silicates. The melt droplets trapped in the silicates crystallize titanomagnetite (Mt), ilmenite, apatite (Ap), hornblende (Hbl), mica and sulfides (Sul). The inset shows a multiphase solid inclusion trapped in an olivine host (not to scale).

intrusion are extremely Fe–Ti-enriched and Si-depleted. They occur within the Lower Zone of the layered sequence, suggesting that the Fe–Ti-rich melts may have formed by immiscible separation at an early stage of the evolution of the ferrobasaltic magma. A similar mechanism has also been used to explain the formation of discordant, plagioclase-absent, Fe–Ti oxide pegmatite in the Bushveld Complex, South Africa (Scoon & Mitchell, 1994).

Downloaded from https://academic.oup.com/petrology/article/55/5/951/1496553 by guest on 20 August 2022

The existence of such immiscible Fe–Ti-rich melts is not well supported by experiments (e.g. Taylor, 1963; Lindsley, 1991, 2003), possibly owing to the fact that experimental reproduction of unmixing is greatly hampered by the masking effects of competing crystallization (Veksler, 2009). However, the discrepancies in magma compositions and physicochemical conditions between experimental simulation in the laboratory and natural magmatic systems allow the possibility of the formation of Fe–Ti-rich, immiscible liquids at a relatively early stage of crystallization. Recent experiments on liquid immiscibility by Lester *et al.* (2013) have found that the presence of H_2O alone or in combination with P, S and F can increase the temperature and compositional range of the miscibility gap, thus favoring liquid–liquid unmixing at an early stage of differentiation. The most Fe-rich melts they obtained contain 7·14 wt % SiO_2, 72·8 wt % FeO and 16·6 wt % S. Fe-rich melts have also been recorded in natural samples such as in melt inclusions within quartz phenocrysts in ignimbrites, which contain 81 wt % FeO^T and 9·9 wt % SiO_2 (Naumov *et al.*, 1993), and globules of Fe oxide-dominated (59–69 wt % FeO^T, 8–11 wt % SiO_2) melts with 10–20% H_2O in igneous xenoliths from the Pliocene–Pleistocene alkali basalts of the Western Carpathians (Hurai *et al.*, 1998). Thus, immiscible separation of extremely Fe–Ti-rich melts may be a common process in some mantle-derived magmas. We speculate that the S, P, F and H_2O contents of the Baima parental magma may have triggered the immiscible separation of Fe–Ti-rich melt at an early stage of magma differentiation, which may explain the occurrence of massive or net-textured Fe–Ti oxide ores in the lower or lower–middle parts of the layered intrusions in the Panxi region.

Liquid immiscibility is an important process in generating diverse magma compositions (e.g. Roedder, 1979). Sulfide melts, for example, result from immiscible separation from a high-temperature basaltic magma and are economically important for concentrating Cu, Ni and PGE. Immiscible nelsonitic melts that form nelsonite associated with massif-type anorthosites are important sources of Fe, Ti and P (Kolker, 1982). Our findings have demonstrated that immiscible processes are also probably responsible for concentrating Fe and Ti in layered mafic intrusions.

CONCLUSIONS

Subspherical to spherical multiphase solid inclusions hosted in olivine within the Fe–Ti oxide ores in the Lower Zone of the Baima intrusion provide strong evidence for the existence of Fe–Ti-rich melts produced by immiscible separation from a ferrobasaltic parent magma at a relatively early stage of magma evolution. This can best explain the presence of massive and net-textured Fe–Ti oxide ores in the lower or lower–middle parts of the layered mafic intrusions in the Panxi area, ELIP. Liquid immiscibility is also likely to be significant in the concentration of Fe–Ti oxides in a variety of geological environments from anorthosites to layered mafic intrusions to volcanic rocks. Fe–Ti-rich melts, with much higher Fe and Ti contents, segregating at an early stage of basaltic magma differentiation should be considered as a possible mechanism for the concentration of economically important Fe, Ti and V ore deposits.

ACKNOWLEDGEMENTS

We are grateful to Professor Yuxiao Ma, Mr Guanghua He and Mr Hong Liu for arranging fieldwork in the Baima mine, and Engineers Shuguang Gui and Xiangshen Xia of the Baima mining company for their help with fieldwork. We thank Mr Tom Bultreys from Ghent University for helping with 3-D CT analyses, Mr Chan Yu Fai Frankie from Electron Microscope Unit, the University of Hong Kong for helping with BSE images and Dr Benxun Su, Dr Jianfeng Gao, Professor Nicholas Arndt and Steve Barnes for helpful discussions. Professor B. Ronald Frost and two anonymous reviewers are gratefully acknowledged for their constructive comments.

FUNDING

This study was supported by a grant from the Research Grant Council of Hong Kong (HKU707012P) to M.-F.Z. Additional support was provided by the CAS/SAFEA International Partnership Program for Creative Research Teams-Intraplate Mineralization Research Team (KZZD-EW-TZ-20).

SUPPLEMENTARY DATA

Supplementary data and videos for this paper are available at *Journal of Petrology* online.

REFERENCES

Bai, Z.-J., Zhong, H., Naldrett, A. J., Zhu, W.-G. & Xu, G.-W. (2012). Whole-rock and mineral composition constraints on the genesis of the giant Hongge Fe–Ti–V oxide deposit in the Emeishan large igneous province, southwest China. *Economic Geology* **107**, 507–524.

Bateman, A. M. (1951). The formation of late magmatic oxide ores. *Economic Geology* **46**, 404–426.

Bowen, N. L. (1922). The reaction principle in petrogenesis. *Journal of Geology* **30**, 177–198.

Bowen, N. L. (1928). *The Evolution of the Igneous Rocks*. Princeton University Press, 334 p.

Brabant, L., Vlassenbroeck, J., De Witte, Y., Cnudde, V., Boone, M. N., Dewanckele, J. & Van Hoorebeke, L. (2011). Three-dimensional analysis of high-resolution X-ray computed tomography data with Morpho+. *Microscopy and Microanalysis* **17**, 252–263.

Charlier, B. & Grove, T. (2012). Experiments on liquid immiscibility along tholeiitic liquid lines of descent. *Contributions to Mineralogy and Petrology* **164**, 27–44.

Downloaded from https://academic.oup.com/petrology/article/55/5/951/1496553 by guest on 20 August 2022

Charlier, B., Duchesne, J. C. & Vander Auwera, J. (2006). Magma chamber processes in the Tellnes ilmenite deposit (Rogaland Anorthosite Province, SW Norway) and the formation of Fe–Ti ores in massif-type anorthosites. *Chemical Geology* **234**, 264–290.

Charlier, B., Sakoma, E., Sauvé, M., Stanaway, K., Vander Auwera, J. & Duchesne, J.-C. (2008). The Grader layered intrusion (Havre-Saint-Pierre Anorthosite, Quebec) and genesis of nelsonite and other Fe–Ti–P ores. *Lithos* **101**, 359–378.

Charlier, B., Namur, O., Toplis, M. J., Schiano, P., Cluzel, N., Higgins, M. D. & Vander Auwera, J. (2011). Large-scale silicate liquid immiscibility during differentiation of tholeiitic basalt to granite and the origin of the Daly gap. *Geology* **39**, 907–910.

Chen, F. W. (1990). Petrologic study on Baima ore-bearing layered mafic–ultramafic intrusion. *Acta Petrologica Sinica* **6**, 12–26 (in Chinese).

Chen, W. T., Zhou, M.-F. & Zhao, T.-P. (2013). Differentiation of nelsonitic magmas in the formation of the ~1·74 Ga Damiao Fe–Ti–P ore deposit, North China. *Contributions to Mineralogy and Petrology* **165**, 1341–1362.

Chung, S.-L. & Jahn, B.-m. (1995). Plume–lithosphere interaction in generation of the Emeishan flood basalts at the Permian–Triassic boundary. *Geology* **23**, 889–892.

Chung, S.-L., Jahn, B. M., Wu, G. Y., Lo, C. H. & Cong, B. L. (1998). The Emeishan flood basalt in SW China: a mantle plume initiation model and its connection with continental break-up and mass extinction at the Permian–Triassic boundary. In: Flower, M. F. J., Chung, S. L., Lo, C. H. & Lee, T. Y. (eds) *Mantle Dynamics and Plate Interaction in East Asia. American Geophysical Union, Geodynamics Series* **27**, 47–58.

Clark, A. H. & Kontak, D. J. (2004). Fe–Ti–P oxide melts generated through magma mixing in the Antauta subvolcanic center, Peru: Implications for the origin of nelsonite and iron oxide-dominated hydrothermal deposits. *Economic Geology* **99**, 377–395.

Dare, S. A. S., Barnes, S.-J. & Beaudoin, G. (2012). Variation in trace element content of magnetite crystallized from a fractionating sulfide liquid, Sudbury, Canada: Implications for provenance discrimination. *Geochimica et Cosmochimica Acta* **88**, 27–50.

Deer, W. A., Howie, R. A. & Zussman, J. (1992). *An Introduction to the Rock-forming Minerals*, 2nd edn. Longman.

Dixon, S. & Rutherford, M. J. (1979). Plagiogranites as late-stage immiscible liquids in ophiolite and mid-ocean ridge suites: An experimental study. *Earth and Planetary Science Letters* **45**, 45–60.

Donaldson, C. H. (1974). Olivine crystal types in harrisitic rocks of the Rhum pluton and in Archean spinifex rocks. *Geological Society of America Bulletin* **85**, 1721–1726.

Duchesne, J. C. (1999). Fe–Ti deposits in Rogaland anorthosites (South Norway): geochemical characteristics and problems of interpretation. *Mineralium Deposita* **34**, 182–198.

Ferrando, S., Frezzotti, M. L., Dallai, L. & Compagnoni, R. (2005). Multiphase solid inclusions in UHP rocks (Su-Lu, China): Remnants of supercritical silicate-rich aqueous fluids released during continental subduction. *Chemical Geology* **223**, 68–81.

Hibbard, M. J. (1981). The magma mixing origin of mantled feldspars. *Contributions to Mineralogy and Petrology* **76**, 158–170.

Holwell, D. A., McDonald, I. & Butler, I. B. (2011). Precious metal enrichment in the Platreef, Bushveld Complex, South Africa: evidence from homogenized magmatic sulfide melt inclusions. *Contributions to Mineralogy and Petrology* **161**, 1011–1026.

Howarth, G. H., Prevec, S. A. & Zhou, M.-F. (2013). Timing of Ti-magnetite crystallisation and silicate disequilibrium in the Panzhihua mafic layered intrusion: Implications for ore-forming processes. *Lithos* **170–171**, 73–89.

Hurai, V., Simon, K., Wiechert, U., Hoefs, J., Konečný, P., Huraiová, M., Pironon, J. & Lipka, J. (1998). Immiscible separation of metalliferous Fe/Ti-oxide melts from fractionating alkali basalt: P–T–fO_2 conditions and two-liquid elemental partitioning. *Contributions to Mineralogy and Petrology* **133**, 12–29.

Hwang, S.-L., Shen, P., Chu, H.-T., Yui, T.-F. & Lin, C.-C. (2001). Genesis of microdiamonds from melt and associated multiphase inclusions in garnet of ultrahigh-pressure gneiss from Erzgebirge, Germany. *Earth and Planetary Science Letters* **188**, 9–15.

Jakobsen, J. K., Veksler, I. V., Tegner, C. & Brooks, C. K. (2005). Immiscible iron- and silica-rich melts in basalt petrogenesis documented in the Skaergaard intrusion. *Geology* **33**, 885–888.

Jakobsen, J. K., Veksler, I. V., Tegner, C. & Brooks, C. K. (2011). Crystallization of the Skaergaard intrusion from an emulsion of immiscible iron- and silica-rich liquids: evidence from melt inclusions in plagioclase. *Journal of Petrology* **52**, 345–373.

Jurek, K. & Hulínský, V. (1980). The use and accuracy of the ZAF correction procedure for the microanalysis of glasses. *Microchimica Acta* **73**, 183–198.

Kamenetsky, V. S., Charlier, B., Zhitova, L., Sharygin, V., Davidson, P. & Feig, S. (2013). Magma chamber-scale liquid immiscibility in the Siberian Traps represented by melt pools in native iron. *Geology* **41**, 1091–1094.

Kent, A. J. R. (2008). Melt inclusions in basaltic and related volcanic rocks. In: Putirka, K. D. & Tepley, F. J., III (eds) *Minerals, Inclusions and Volcanic Processes. Mineralogical Society of America and Geochemical Society, Reviews in Mineralogy and Geochemistry* **69**, 273–331.

Kolker, A. (1982). Mineralogy and geochemistry of Fe–Ti oxide and apatite (nelsonite) deposits and evaluation of the liquid immiscibility hypothesis. *Economic Geology* **77**, 1146–1158.

Lester, G. W., Clark, A. H., Kyser, T. K. & Naslund, H. R. (2013). Experiments on liquid immiscibility in silicate melts with H_2O, P, S, F and Cl: implications for natural magmas. *Contributions to Mineralogy and Petrology* **166**, 329–349.

Lindsley, D. H. (1991). Experimental studies of oxide minerals. In: Lindsley, D. H. (ed.) *Oxide Minerals. Mineralogical Society of America, Reviews in Mineralogy* **25**, 69–106.

Lindsley, D. H. (2003). Do Fe–Ti oxide magma exist? Geology: yes; Experiment: no! *NGU Special Publication* **9**, 34–35.

Lister, G. F. (1966). The composition and origin of selected iron–titanium deposits. *Economic Geology* **61**, 275–310.

Liu, P.-P., Zhou, M.-F., Wang, C. Y., Xing, C.-M. & Gao, J.-F. (2014). Open magma chamber processes in the formation of the Permian Baima mafic–ultramafic layered intrusion, SW China. *Lithos* **184–187**, 194–208.

Liu, Y., Hu, Z., Gao, S., Günther, D., Xu, J., Gao, C. & Chen, H. (2008). *In situ* analysis of major and trace elements of anhydrous minerals by LA-ICP-MS without applying an internal standard. *Chemical Geology* **257**, 34–43.

Loferski, P. & Arculus, R. (1993). Multiphase inclusions in plagioclase from anorthosites in the Stillwater Complex, Montana: implications for the origin of the anorthosites. *Contributions to Mineralogy and Petrology* **114**, 63–78.

Ma, Y. X., Ji, X. T., Li, J. C., Huang, M. & Min, Z. Z. (2003). *Mineral resources of Panzhihua, Sichuan Province, SW China*. Chengdu University of Technology (in Chinese).

Masschaele, B. C., Cnudde, V., Dierick, M., Jacobs, P., Van Hoorebeke, L. & Vlassenbroeck, J. (2007). UGCT: New X-ray radiography and tomography facility. *Nuclear Instruments and Methods in Physics Research, Section A* **580**, 266–269.

McCarthy, T. S., Cawthorn, R. G., Wright, C. J. & McIver, J. R. (1985). Mineral layering in the Bushveld Complex; implications

Downloaded from https://academic.oup.com/petrology/article/55/5/951/1496553 by guest on 20 August 2022

of Cr abundances in magnetite from closely spaced magnetitite and intervening silicate-rich layers. *Economic Geology* **80**, 1062–1074.

McDonough, W. F. & Sun, S. S. (1995). The composition of the Earth. *Chemical Geology* **120**, 223–253.

Naldrett, A. J. (1999). World-class Ni–Cu–PGE deposits: key factors in their genesis. *Mineralium Deposita* **34**, 227–240.

Namur, O., Charlier, B. & Holness, M. B. (2012). Dual origin of Fe–Ti–P gabbros by immiscibility and fractional crystallization of evolved tholeiitic basalts in the Sept Iles layered intrusion. *Lithos* **154**, 100–114.

Nash, W. P. (1976). Fluorine, chlorine, and OH-bearing minerals in the Skaergaard Intrusion. *American Journal of Science* **276**, 546–556.

Naslund, H. R. (1983). The effect of oxygen fugacity on liquid immiscibility in iron-bearing silicate melts. *American Journal of Science* **283**, 1034–1059.

Naumov, V. B., Solovova, I. P., Kovalenker, V. A. & Rusinov, V. L. (1993). Immiscibility in acidic magmas: evidence from melt inclusions in quartz phenocrysts of ignimbrites. *European Journal of Mineralogy* **5**, 937–941.

Pang, K. N., Li, C. S., Zhou, M. F. & Ripley, E. M. (2008*a*). Abundant Fe–Ti oxide inclusions in olivine from the Panzhihua and Hongge layered intrusions, SW China: evidence for early saturation of Fe–Ti oxides in ferrobasaltic magma. *Contributions to Mineralogy and Petrology* **156**, 307–321.

Pang, K. N., Zhou, M. F., Lindsley, D., Zhao, D. & Malpas, J. (2008*b*). Origin of Fe–Ti oxide ores in mafic intrusions: Evidence from the Panzhihua intrusion, SW China. *Journal of Petrology* **49**, 295–313.

Pang, K. N., Li, C. S., Zhou, M. F. & Ripley, E. M. (2009). Mineral compositional constraints on petrogenesis and oxide ore genesis of the late Permian Panzhihua layered gabbroic intrusion, SW China. *Lithos* **110**, 199–214.

Park, J.-W., Campbell, I. H., Ickert, R. B. & Allen, C. M. (2013). Chalcophile element geochemistry of the Boggy Plain zoned pluton, southeastern Australia: a S-saturated barren compositionally diverse magmatic system. *Contributions to Mineralogy and Petrology* **165**, 217–236.

Philpotts, A. R. (1967). Origin of certain iron–titanium oxide and apatite rocks. *Economic Geology* **62**, 303–315.

Reynolds, I. M. (1985*a*). Contrasted mineralogy and textural relationships in the uppermost titaniferous magnetite layers of the Bushveld Complex in the Bierkraal area north of Rustenburg. *Economic Geology* **80**, 1027–1048.

Reynolds, I. M. (1985*b*). The nature and origin of titaniferous magnetite-rich layers in the upper zone of the Bushveld Complex; a review and synthesis. *Economic Geology* **80**, 1089–1108.

Ripley, E. M., Severson, M. J. & Hauck, S. A. (1998). Evidence for sulfide and Fe–Ti–P-rich liquid immiscibility in the Duluth Complex, Minnesota. *Economic Geology* **93**, 1052–1062.

Roedder, E. (1979). Silicate liquid immiscibility in magmas. In: Yoder, H. S. (ed.) *The Evolution of the Igneous Rocks: Fiftieth Anniversary Perspectives*. Princeton University Press, pp. 15–58.

Roedder, E. & Weiblen, P. W. (1970). Silicate liquid immiscibility in lunar magmas, evidenced by melt inclusions in lunar rocks. *Science* **167**, 641–644.

Schiano, P., Clocchiatti, R., Lorand, J.-P., Massare, D., Deloule, E. & Chaussidon, M. (1997). Primitive basaltic melts included in podiform chromites from the Oman Ophiolite. *Earth and Planetary Science Letters* **146**, 489–497.

Scoon, R. N. & Mitchell, A. A. (1994). Discordant iron-rich ultramafic pegmatites in the Bushveld Complex and their relationship to iron-rich intercumulus and residual liquids. *Journal of Petrology* **35**, 881–917.

Shellnutt, J. & Pang, K.-N. (2012). Petrogenetic implications of mineral chemical data for the Permian Baima igneous complex, SW China. *Mineralogy and Petrology* 1–14.

Sichuan Bureau of Geology and Mineral Resources. (2007). *Report of resource reserve of Baima oxide ore deposit in Miyi, Sichuan Province*. SBGMR.

Song, X. Y., Zhou, M. F., Hou, Z. Q., Cao, Z. M., Wang, Y. L. & Li, Y. G. (2001). Geochemical constraints on the mantle source of the upper Permian Emeishan continental flood basalts, southwestern China. *International Geology Review* **43**, 213–225.

Song, X.-Y., Keays, R. R., Xiao, L., Qi, H.-W. & Ihlenfeld, C. (2009). Platinum-group element geochemistry of the continental flood basalts in the central Emeisihan Large Igneous Province, SW China. *Chemical Geology* **262**, 246–261.

Song, X.-Y., Qi, H.-W., Hu, R.-Z., Chen, L.-M., Yu, S.-Y. & Zhang, J.-F. (2013). Formation of thick stratiform Fe–Ti oxide layers in layered intrusion and frequent replenishment of fractionated mafic magma: Evidence from the Panzhihua intrusion, SW China. *Geochemistry, Geophysics, Geosystems* **14**, 712–732.

Sparks, H. A. & Mavrogenes, J. A. (2005). Sulfide melt inclusions as evidence for the existence of a sulfide partial melt at Broken Hill, Australia. *Economic Geology* **100**, 773–779.

Taylor, R. W. (1963). Liquidus temperatures in the system FeO–Fe_2O_3–TiO_2. *Journal of the American Ceramic Society* **46**, 276–279.

Tepley, F. J., Davidson, J. P. & Clynne, M. A. (1999). Magmatic interactions as recorded in plagioclase phenocrysts of Chaos Crags, Lassen Volcanic Center, California. *Journal of Petrology* **40**, 787–806.

Toplis, M. J. & Carroll, M. R. (1996). Differentiation of ferro-basaltic magmas under conditions open and closed to oxygen: implications for the Skaergaard intrusion and other natural systems. *Journal of Petrology* **37**, 837–858.

VanTongeren, J. A. & Mathez, E. A. (2012). Large-scale liquid immiscibility at the top of the Bushveld Complex, South Africa. *Geology* **40**, 491–494.

Veksler, I. V. (2009). Extreme iron enrichment and liquid immiscibility in mafic intrusions: Experimental evidence revisited. *Lithos* **111**, 72–82.

Veksler, I. V., Dorfman, A. M., Borisov, A. A., Wirth, R. & Dingwell, D. B. (2007). Liquid immiscibility and the evolution of basaltic magma. *Journal of Petrology* **48**, 2187–2210.

Vlassenbroeck, J., Dierick, M., Masschaele, B., Cnudde, V., Van Hoorebeke, L. & Jacobs, P. (2007). Software tools for quantification of X-ray microtomography at the UGCT. *Nuclear Instruments and Methods in Physics Research, Section A* **580**, 442–445.

Von Gruenewaldt, G. (1993). Ilmenite–apatite enrichments in the Upper Zone of the Bushveld Complex: a major titanium–rock phosphate resource. *International Geology Review* **35**, 987–1000.

Wager, L. R. & Brown, G. M. (1968). *Layered Igneous Rock*. Edinburgh: Oliver & Boyd, 588 p.

Wang, C. Y. & Zhou, M.-F. (2013). New textural and mineralogical constraints on the origin of the Hongge Fe–Ti–V oxide deposit, SW China. *Mineralium Deposita* 1–12.

Wang, C. Y., Zhou, M. F. & Qi, L. (2007). Permian flood basalts and mafic intrusions in the Jinping (SW China) Song Da (northern Vietnam) district: Mantle sources, crustal contamination and sulfide segregation. *Chemical Geology* **243**, 317–343.

Xiao, L., Xu, Y. G., Mei, H. J., Zheng, Y. F., He, B. & Pirajno, F. (2004). Distinct mantle sources of low-Ti and high-Ti basalts from the western Emeishan large igneous province, SW China: implications for plume–lithosphere interaction. *Earth and Planetary Science Letters* **228**, 525–546.

Downloaded from https://academic.oup.com/petrology/article/55/5/951/1496553 by guest on 20 August 2022

Xu, Y., Chung, S.-L., Jahn, B.-m. & Wu, G. (2001). Petrologic and geochemical constraints on the petrogenesis of Permian–Triassic Emeishan flood basalts in southwestern China. *Lithos* **58**, 145–168.

Zhang, X.-Q., Song, X.-Y., Chen, L.-M., Xie, W., Yu, S.-Y., Zheng, W.-Q., Deng, Y.-F., Zhang, J.-F. & Gui, S.-G. (2012). Fractional crystallization and the formation of thick Fe–Ti–V oxide layers in the Baima layered intrusion, SW China. *Ore Geology Reviews* **49**, 96–108.

Zhang, X.-Q., Song, X.-Y., Chen, L.-M., Yu, S.-Y., Xie, W., Deng, Y., Zhang, J.-F. & Gui, S.-G. (2013). Chalcophile element geochemistry of the Baima layered intrusion, Emeishan Large Igneous Province, SW China: implications for sulfur saturation history and genetic relationship with high-Ti basalts. *Contributions to Mineralogy and Petrology* 1–17.

Zhou, M.-F., Malpas, J., Song, X., Kennedy, A. K., Robinson, P. T., Sun, M., Lesher, C. M. & Keays, R. R. (2002). A temporal link between the Emeishan large igneous province (SW China) and the end-Guadalupian mass extinction. *Earth and Planetary Science Letters* **196**, 113–122.

Zhou, M.-F., Robinson, P. T., Lesher, C. M., Keays, R. R., Zhang, C. J. & Malpas, J. (2005). Geochemistry, petrogenesis and metallogenesis of the Panzhihua gabbroic layered intrusion and associated Fe–Ti–V oxide deposits, Sichuan Province, SW China. *Journal of Petrology* **46**, 2253–2280.

Zhou, M.-F., Arndt, N. T., Malpas, J., Wang, C. Y. & Kennedy, A. K. (2008). Two magma series and associated ore deposit types in the Permian Emeishan large igneous province, SW China. *Lithos* **103**, 352–368.

Zhou, M.-F., Chen, W. T., Wang, C. Y., Prevec, S. A., Liu, P. P. & Howarth, G. H. (2013). Two stages of immiscible liquid separation in the formation of Panzhihua-type Fe–Ti–V oxide deposits, SW China. *Geoscience Frontiers* **4**, 479–620.

Downloaded from https://academic.oup.com/petrology/article/55/5/951/1496553 by guest on 20 August 2022